STAR FORMATION RATE INDICATORS IN THE FIRE SIMULATIONS & SPT 2349-56: A MASSIVE AND ACTIVE PROTO-CLUSTER CORE

by

Timothy B. Miller

Submitted in partial fulfillment of the requirements
for the degree of Master of Science

at

Dalhousie University
Halifax, Nova Scotia
July 2017

Table of Contents

List of Tables

List of Figures

Abstract

Part 1)

When studying galaxies, the star formation rate (SFR) is an important diagnostic as it gives insight into the evolutionary stage of the galaxy. Young galaxies will be actively forming stars and growing quickly, while older, quiescent galaxies will have low SFRs. The total infrared (IR) luminosity of a galaxy is a commonly used tracer of SFR. A simple radiative transfer model to estimate the IR luminosity of hydrodynamic simulations of galaxies is presented. This algorithm is then applied to the feedback in realistic environments (FIRE) simulation suite. The IR luminosity is then compared directly to the SFR, which is known in the simulations. These results are compared to a well established model. The model is found to have a bias that systematically overestimates the SFR of a galaxy. A large amount of scatter also cautions against the interpretations of observations from this simple model.

Part 2)

The most massive galaxies formed quickly in the early Universe and today reside in rich galaxy clusters. Studying progenitors of galaxy clusters (proto-clusters) presents an exciting opportunity to study star formation in extreme environments in the early universe. High resolution sub-mm imaging of the proto-cluster SPT 2349-56 is presented. SPT 2349-56 contains 12 gas rich and star forming galaxies in an extremely confined radius of $\sim 12''$. The high velocity dispersion of these galaxies and enormous gas and star formation densities suggest SPT 2349-56 represents the core of an especially active and massive proto-cluster. Comparison with other known proto-cluster systems shows that SPT 2349-56 is truly unique.

List of Abbreviations and Symbols Used

ALMA	Atacama large millimeter array
AGN	Active galactic nuclei
LABOCA	Large APEX bolometer array camera
SPT	South pole telescope
SMG	Sub-millimetre galaxy
SED	Spectral energy distribution
SFR	Star formation rate
SFH	Star formation history
SFRD	Star formation rate density
SNR	Signal-to-noise ratio
SPH	Smoothed particle hydrodynamics
IR	Infrared
UV	Ultraviolet
z	Redshift
$\odot$	Solar units
$L_\odot$	Solar luminosity
$M_\odot$	Solar mass
M_*	Stellar mass
$'$	Arcminute
$''$	Arcsecond
Jy	Jansky
pc	Parsec
ISM	Inter-stellar Medium
IMF	Initial Mass function
Z	Metallicity
L_{bol}	Bolometric luminosity
L_{IR}	Infrared luminosity
dex	order of magnitude
SN	supernova

Acknowledgements

First and foremost I would like the thank my supervisor Scott Chapman. He has provided me with incredible opportunities and I look forward to continuing to work with him in the future. I would also like to thank Chris Hayward and Phil Hopkins who graciously hosted and supervised me during my year long stay at Caltech.

My lab mates Kevin Lacaille, Kaja Rotermund, Colin Ross and Ryan Perry along with fellow basement dwellers Simon Meynell, David Kalliecharan for many useful discussions and endless motivation.

Finally my family and many other friends for their never ending love and support.

Chapter 1

Introduction

1.1 Galaxy Formation

By its most basic definition, a galaxy is a dynamically bound system of gas, stars and dark matter. Typical galaxies, like our own Milky Way, contain tens of billions of individual stars and about one tenth of that mass in gas. They represent beacons in a mostly dark and empty universe. They are a fascinating and diverse class of astrophysical objects. Galaxies come in many shapes and sizes and have existed in the universe since a mere 500 Myr after the big bang (The current age of the universe is $\sim$ 13.7 Gyr). The study of how galaxies form and evolve is known as galaxy formation. Physical principles from fluid dynamics, radiative transfer, cosmology and many other fields are combined to further our understanding. This field has made incredible leaps in the past several decades due to increasingly powerful telescopes and improving theoretical models yet, much is still unknown.

1.1.1 Galaxy Constituents

Although galaxies come in all shapes and sizes, there are characteristics all of them posses. Sizes range from 5 to 20 kpc[1] while typical separations between galaxies are on the order of a few Megaparsecs. Every galaxy is made up of three basic constituents: dark matter, gas and stars. Dark matter makes up the bulk of the mass of a galaxy and is responsible for keeping the stars and gas gravitationally bound. The gas, primarily hydrogen, is spread throughout the galaxy. When the gas reaches a sufficient density it collapses upon itself to form stars. Stars emit light and allow us to observe galaxies. This 3-component description helps us understand some of the

[1] 1 parsec (pc) = 3.09×10^{16} m = 3.26 light years

physical processes that shape galaxies.

Dark matter represents about 80% of the total mass of the universe and governs its large-scale dynamics. Peaks in the dark matter distribution are known as halos. Galaxies reside within these dark matter halos. They originated in the early universe and grew by gravitational attraction since they were denser than the surroundings regions. The characteristic mass and radius of a halo is the virial radius (R_{vir}) and virial mass (M_{vir}). These are defined by the virial theorem, which relates the kinetic energy of a group of particles to the potential energy that binds them together [74]. The dark matter halo is the backbone on which the rest of the galaxy is built.

As the halo grows it accretes gas along with dark matter. The gas in galaxies is comprised of $\sim 90\%$ hydrogen, $\sim 10\%$ helium and trace amounts of metals. Metals are defined as anything heavier than helium. The most abundant of the metals are carbon and oxygen, as they are by-products of the hydrogen fusion process which powers stars. The amount of metals in a galaxy is characterized by the metallicity, Z. This is the mass ratio of metals to hydrogen and helium. Gas in galaxies is extremely turbulent and covers a range of densities from 10^{-1} molecules cm^{-3} to 10^{3} molecules cm^{-3} and temperatures from 10 K to 10^{6} K. Along with gas, metals also appear in the form carbonaceous and silicate grains known as cosmic dust. These grains have an average radius of $\sim$ 1 μm. They have an extremely large absorption cross section in the ultraviolet (UV) and visible regions of the electromagnetic spectrum [34]. This dust is thermally decoupled from the gas and has a much lower temperature of 30 K - 50 K [21]. Gas and dust together make up the inter-stellar medium (ISM) of galaxies.

As the gas is accreted on to the halo, it cools and falls into the center. The cooling time of the in-falling gas is much shorter than the free-fall time therefore the gas is cool when it reaches the centre of the halo. Typically the vast majority of gas exists within the inner $\frac{1}{10}$ R_{vir} of the halo. Although the dark matter makes up the bulk of the mass for the entire halo, in this central region the dynamics are dominated by the gas. This gas continues to cool and fragments into self-gravitating clouds. The main cooling mechanism in dense gas is the recombination of collisionally excited atoms

or molecules [82]. The kinetic energy of these collisions is converted into radiation. Therefore, cooling becomes more efficient as the density of gas increases. Individual clouds have masses of 10^5 $M_\odot$ - 10^6 $M_\odot$. [2] [68] Stars form when gas within these clouds catastrophically collapses. This is not an instant process and takes on the order of 1 Myr.

Stars are the shining beacons that allow us to observe galaxies. When they are young, i.e. less than 100 Myr old, stars are the at peak temperature and luminosity. During this period, they emit the most power in the UV spectral region. The most massive stars ($M > 10$ $M_\odot$) only exist for around $\sim$ 50 Myr until they explode in supernovae (SN). These thermo-nuclear explosions impart over 10^{40} J of energy back into the ISM [47]. Other feedback mechanisms such as radiation pressure also impart momentum onto the surrounding gas. SN and other feedback mechanisms help stars disrupt the gas clouds they were born in. This happens on a times scale of $\sim$ 100 Myr. At it's most extreme, these feedback mechanisms can also create outflows which expel significant fractions of gas from the galaxy [72]. Less massive stars outlive their birth clouds. As they age, they cool causing the peak emission to shift from the UV into the visible and near-IR regions of the spectrum and their luminosity decreases. Feedback from old stars is much less impactful than their younger counterparts.

1.1.2 Evolution

Before the evolution of galaxies is discussed, the concept of redshift will be introduced. Redshift is the reddening of observed spectra due to the doppler shift caused by the expanding universe. This idea is encapsulated in the equation below.

$$z = \frac{\lambda_{\text{obs}}}{\lambda_{\text{rest}}} - 1 \tag{1.1}$$

z is the measured redshift, λ_{obs} is the observed wavelength and λ_{rest} is the wavelength of rest-frame emission. The longer light is traveling the more redshift it will experience due to the expansion of the universe. The longer travel time corresponds to a larger

[2] $\odot$ refers to solar units, i.e. $M_\odot$ is the mass of the sun.

distance due to the finite speed of light. Objects with a higher redshift are older and further away. Redshift zero represents the local, present universe, $z = 1$ is when the universe was 5.9 Gyr old, approximately half as old as it is now. There is a non-linear relation between redshift and time which follows an approximately $t^{-3/2}$ scaling. The redshift of an object, z, is used as an analog for both its age and distance.

The amount of star formation in a galaxy is characterized by the star formation rate (SFR). This is a measure of the rate that new stars are forming. It is a useful measure to identify the evolutionary state of galaxies. Since the process of gas collapsing and turning into stars takes ~ 1 Myr, an 'instantaneous' star formation rate is not physically plausible and time averaged measures are used [60]. For example, sum the total mass of stars that formed within the past 100 Myr and divide by 100 Myr. The result is the average SFR over the past 100 Myr. If the total mass of young stars is known the SFR of a galaxy can be estimated. From stellar population models the mass to light ratio of stars is known therefore the mass of young stars can be calculated from their luminosity. The key is to distinguish the light from young stars from old stars. A common measure of SFR is the UV luminosity [88]. Young and hot stars shine bright in the UV and older, cooler stars do not. By observing the UV luminosity of a galaxy, we are selectively measuring the young stars and can estimate their mass and the SFR of the galaxy. Another common measure is the infrared (IR) luminosity, which will be described in detail below.

The evolution of the SFR density (SFRD) across the age of the universe is shown in Figure 1.1. This figure is taken from Madau & Dickinson (2014) [71] and shows a compilation of SFR density measurements spanning almost the entire age of the universe. This is the SFR density of the universe and is calculated by totaling the SFR of all galaxies within a given representative volume. In the early, high redshift universe the SFRD rises to reach a maximum at around $z = 2.5$. This period, $2 < z < 3$, is known as the epoch of peak formation. During this time, the majority of stellar mass in the universe is built up. After this epoch, the SFRD begins to decline, and continues to until the present day.

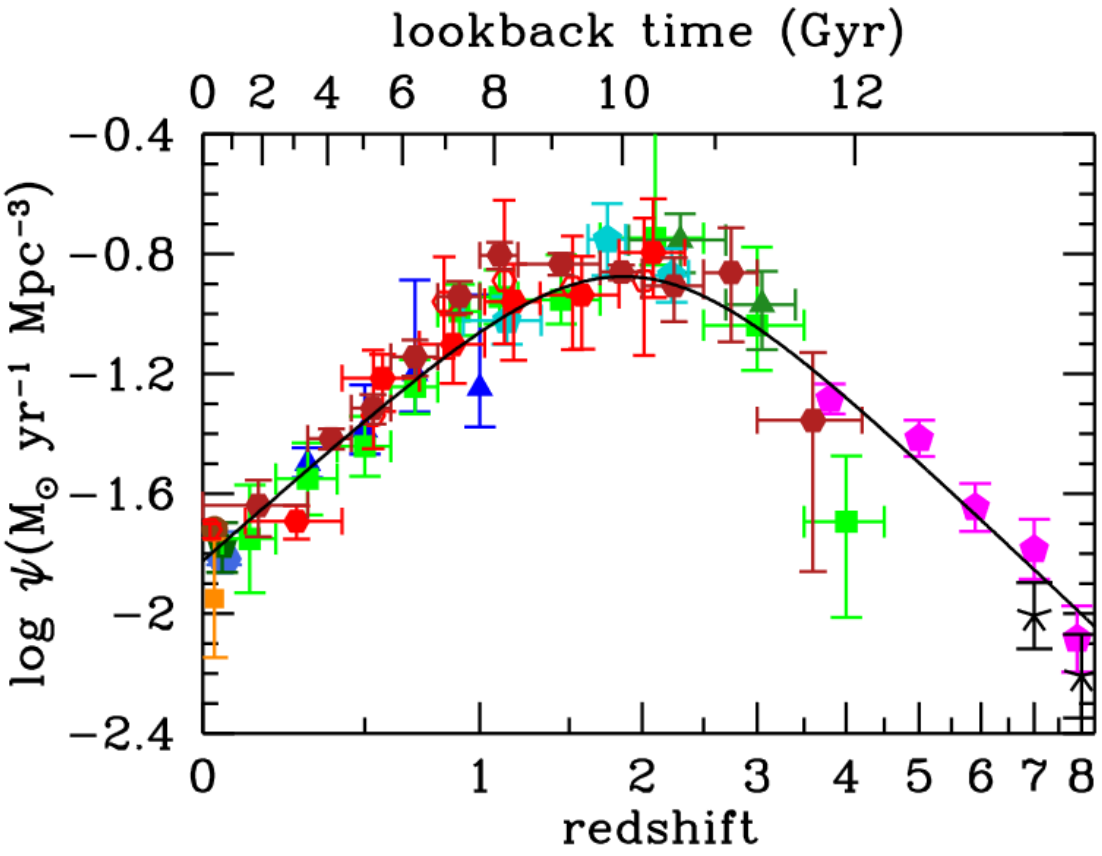

Figure 1.1: This figure displays the cosmic star formation rate density as a function of redshift and time. It is taken from Madau & Dickinson (2014) [71]. A strong peak emerges at $z \sim 2$, this is known as the epoch of peak formation.

There are many physical processes thought to contribute to the shape of the cosmic SFRD. In the early universe, the rise in star formation is thought to be related to the growth of mass in halos. As halos grow and continue to accrete gas, there is more available to form stars [3]. However, this process takes time, and thus the SFRD rises with time as more gas falls onto galaxies. Several processes likely contribute to the decline of star formation at $z < 2$. Feedback from young stars and active galactic nuclei (AGN) works to inhibit star formation [89]. AGN are produced by gas accreting onto a super massive black hole in the center of the galaxy and are extremely luminous across the electromagnetic spectrum from the radio up to gamma rays. This radiation continually heats gas in the galaxy disrupting clouds and suppressing star

formation. At $z < 1$ gas reservoirs of galaxies have also been depleted leaving nothing to form stars from. Many physical processes likely contribute to the shape SFRD as a function of time, but a complete explanation does not exist.

Although the evolution of the cosmic SFRD is smooth, the evolution of individual galaxies is certainly not. Each galaxy is a unique system and there is a lot of variation in the star formation histories (SFHs), thus only general statements can be made. There is often a rise in SFR during the early stages, as the halo is growing, but this is not necessarily monotonic. Then the galaxy may go through burst and quench cycles [94]. Bursts are periods of extremely high SFR, compared to when a galaxy is not forming stars or quenched. The difference in SFR between these two regimes can be multiple orders of magnitude. An individual galaxy can go through dozens of these cycles. This cyclic nature is driven by feedback from young stars. After new stars are formed, the energy imparted from SN, radiation pressure etc. disrupts the gas such that it cannot form stars. The stars then age and the feedback becomes less impactful. The gas can then cool and collapses into clouds again. New stars are then formed and the cycle repeats. Burst/quench cycles are more pronounced in smaller galaxies because when this feedback is triggered, a larger fraction of the gas is disrupted [49]. In more massive galaxies it is difficult for a single population of new stars to have a dramatic effect on the dynamics of the entire galaxy, therefore they tend to have smoother star formation histories. This cycle eventually ends when there is no gas remaining to form stars or the galaxies grows to a sufficient size. The chaotic nature of stellar feedback and gas dynamics leads to incredibly variable star formation histories.

1.1.3 Galaxy clusters

Galaxies show a strong tendency to cluster into groups. The largest of these groups are known as galaxy clusters. With masses greater than 10^{15} $M_{\odot}$, clusters in the local universe are the largest gravitationally bound structures observed. These colossal objects spread over several megaparsecs and contain hundreds to thousands of galaxies.

The extreme nature of galaxy clusters makes them an ideal laboratory for testing astrophysical theories. Not only for galaxy formation but also cosmology. Their number density and properties have helped distinguish between different models of cosmological evolution. Clusters are often characterized by their overdensity. This is a unitless measure of how much more of a given quantity (i.e. dark matter, number of galaxies etc.) there is in a given volume compared to what is expected. Any viable theory of galaxy formation or cosmology must adequately explain the properties of clusters.

Due to their importance to our understanding of galaxy formation, there has been significant study of the progenitors of galaxy clusters: proto-clusters. Although often loosely defined, a proto-cluster is a direct progenitor of a local galaxy cluster. In other words, a system that at $z = 0$ will have a halo mass of $\sim 10^{15}$ $M_{\odot}$. Theoretical studies of proto-clusters reveal that at $z > 2$ they are extended, often beyond 10 Mpc and not gravitationally bound [26]. The galaxy overdensity is also less pronounced in the early universe. Unfortunately, this makes proto-clusters difficult to detect. There are several examples of observed proto-clusters at $z > 2$ however it is not a complete sample and based mostly on serendipitous detections [81, 20]. The study of proto-clusters is crucial to our understanding of galaxy formation; however, we still do not have a complete sample to study.

Figure 1.2 displays the evolution of a galaxy cluster in the cosmological simulation Illustris [110]. At $z = 4$ the cluster is significantly extended on scales of ~ 10 Mpc with much less pronounced gas and dark matter over densities. At this point it is still considered a proto-cluster. As it evolves, gravitational attraction drags dark matter and gas to the center of the cluster. By $z = 0$ there is a huge over density in the central region surround by relative voids. At all points in the evolution the gas, and therefore galaxies, trace the dark matter distribution well. The gas temperature and metallicity are highest at the center of the cluster and grow as time evolves. Clusters represent the largest overdensities of dark matter, gas and galaxies in the universe.

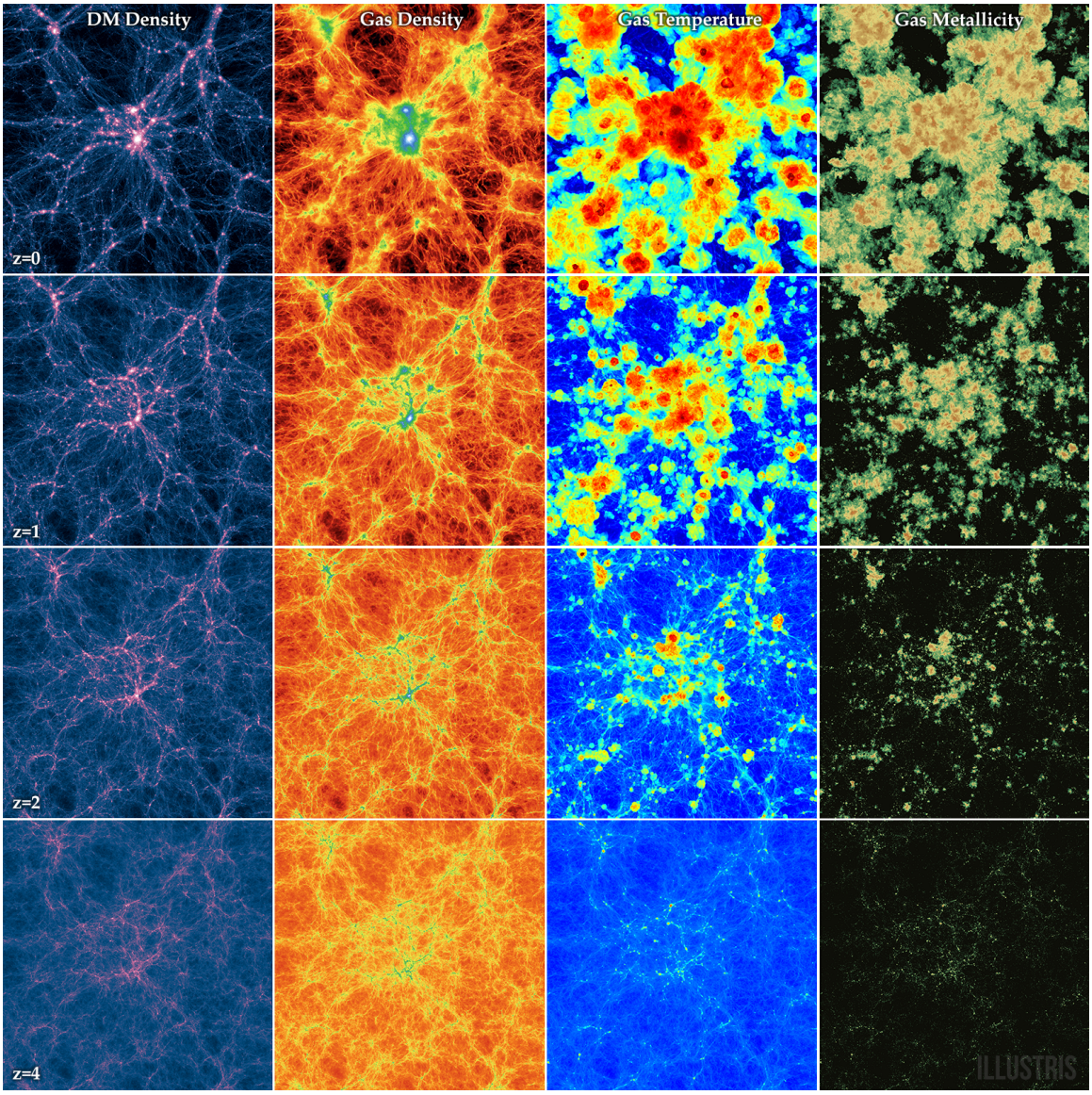

Figure 1.2: This figure shows the evolution of a galaxy cluster in the Illustris simulation [110]. Each panel has a side length of $\sim$ 100 Mpc. Dark matter density, gas density, temperature and metallicity are shown evolving from redshift four to zero. In earlier epochs, the cluster is less pronounced and more extended.

1.2 Infrared Emission from Galaxies

Electromagnetic radiation is how galaxies are observed and interpreted. They emit at many wavelengths spanning the entire electromagnetic spectrum. The spectrum of luminosity vs. wavelength is known as the spectral energy distribution (SED). Studying the SED of galaxies allows astronomers to characterize galaxies and provides insight into the physical processes which govern them. At short wavelengths ($\lambda <$ 1 μm) a galaxy's SED is dominated by direct light from stars [78]. As discussed, younger hotter stars emit most strongly in the UV and older stars emit strongly at longer wavelengths in the visible and near IR regions. However there is essentially zero emission below $\lambda = 91.2$ nm. This wavelength corresponds to an energy of 13.6 eV, the ionization energy of neutral hydrogen. The abundance of neutral hydrogen in the ISM means any photon more energetic than the ionization energy will be almost instantly absorbed [99]. The focus of this study is the infrared (IR) region of the spectrum. This is the region from wavelengths of 8 μm to 1000 μm. Emission from galaxies in the IR is almost entirely thermal emission from dust in the ISM.

1.2.1 Dust continuum

Although dust makes up a small fraction of mass in the ISM, it dominates the absorption properties. These complex molecules are extremely efficient at absorbing light in the UV to visible spectral regions and re-emit it in the IR. Unfortunately, this is an extreme hindrance to astronomers wishing to observe galaxies at these wavelengths. The dust emits thermally, at a much longer wavelength as the temperature dust in galaxies ranges from 30K - 50K [13]. According to a blackbody spectrum, the thermal emission peaks between 50 μm and 100 μm. The ISM has very low absorption in this region of the spectrum, therefore the thermal radiation streams freely out of the galaxy. Although dust impedes that observation of galaxies at short wavelength, it opens a new window to study them in the IR.

Thermal emission from dust in galaxies is often characterized as a modified blackbody. This is shown in the equation below.

$$S(\nu, T) \propto \nu^{\beta} B(\nu, T) \propto \frac{\nu^{3+\beta}}{e^{\frac{h\nu}{k_b T}} - 1} \tag{1.2}$$

Where $S(\nu, T)$ is the flux emitted a a given frequency ν and characteristic dust temperature T. h and k_b are Planck's and Boltzmann's constants and β is the dust emissivity index. β is often assumed to be 1.5. The modified black body fits the IR SED well at wavelength's greater than 50 μm [19]. At shorter wavelengths, it underestimates the observed SEDs. This is thought to be the result of hot dust subcomponents with $T > 80$K. Some studies have suggested alternative fitting functions such as piecewise blackbody and power law function to better fit the IR SED at $\lambda < 50$ μm [7]. However, these are empirical fits and not physically motivated. The IR SED of galaxies is generally well described by a modified blackbody at a characteristic dust temperature.

In his seminal work, Kennickutt (1998) ([58], hereafter K98) proposed using the total infrared luminosity, L_{IR}, as a tracer of SFR. The key insight is that only young stars contribute to dust heating. Stars are born in dense gas clouds where the optical depth of dust is much greater than one. In this picture, essentially all the radiation emitted by young stars is absorbed. This radiation heats the dust which then begins to emit thermally. As the stars age and their birth cloud is dispersed the optical depth of dust begins to decrease. By the time stars reach 100 Myr old, the birth cloud is completely disrupted and the optical depth of dust is thought to be vanishingly small. Therefore, radiation from stars older than 100 Myr is not absorbed and does not contribute to heating the dust. Only young stars contribute to dust heating which then re-radiates all the luminosity absorbed in the IR. Assuming the dust is in thermal equilibrium, the total luminosity emitted is equal to the total luminosity absorbed. Therefore, the total luminosity emitted in the IR is equal to the total luminosity emitted from young stars. Using stellar population models, a mass to light ratio for stars can be estimated. From L_{IR}, the mass of young stars can be

estimated. Assuming a timescale of 100 Myr, SFR can then be calculated. As traced by L_{IR}, SFR is implicitly averaged over 100 Myr. The conclusion drawn in K98 is that there is a linear relationship between L_{IR} and SFR.

Although the K98 conversion is extremely useful and still widely used today, there are a set of caveats when it is used to measure SFR. Firstly, all the luminosity emitted from young is assumed to be absorbed. This is true in almost all cases as stars are born in a dense gas cloud. It is possible that through a merger, or series of SN explosions that a galaxy can be depleted of its gas and dust reservoir. When this occurs, the optical depth of dust may be sufficiently low that not all light from young stars will be absorbed. In this case L_{IR}would underestimate the SFR. Another assumption is that stars older then 100 Myr do not contribute to dust heating. If old stars contribute significantly to dust heating, L_{IR} will overestimate SFR. In the ideal case L_{IR} directly traces only young stars but it may not always be this simple.

There is an implicit time averaging when using L_{IR} to trace SFR since stars take $\sim$ 100 Myr to shed their birth clouds. This leads to another assumption that new stars should be forming at a relatively constant rate over the previous 100 Myr. The stellar population models used to calculate the conversion factor assume a constant SFR over the past 100 Myr. If the number of new stars formed is skewed to the beginning or the end of this 100 Myr, a different conversion factor would be required. For example, if there is a large population of stars with an age of 90 Myr that are less luminous than younger stars, L_{IR} would likely underestimate the SFR. Another implicit assumption is the distribution of masses of new stars that are born. This is known as the initial mass functions (IMF). The IMF affects the L_{IR} to SFR conversion by changing the mass to light ratio produced by stellar population models. Along with the IMF, more advanced stellar populations models used are the major differences between the original model and current conversion factors [59]. There are presently two commonly used IMF: Charbrier [23] and Kroupa [63]. This difference only affects the conversion factor by $\pm$30%. Even with these major assumptions the K98 L_{IR} to SFR conversion is widely used by many studies to estimate the SFR of galaxies.

1.2.2 Emission lines

On top of the dust continuum, there are also emission lines present in the IR. These occur when atoms or molecules in the ISM spontaneously decay from an excited state. Emission lines always occur at the same rest frequency and are broadened by the motion of gas in the galaxy. They give useful insight into the physical conditions of the ISM. Temperature and density of gas in the ISM can be probed by comparing the strengths of different lines. Two of the predominant lines in the IR are [CII] from ionized carbon and the rotational transitions of carbon monoxide.

[CII] is the brightest emission line in the IR and is the dominant coolant of gas in the ISM. Ionized carbon has a low excitation energy of 11.2 eV and is therefore widely present in the ISM. [CII] is the result of the $^2P_{3/2} \rightarrow {}^2P_{1/2}$ electronic transition in ionized carbon and emits a photon at 157.7 μm. The ionized carbon atoms are excited through collisions with neutral hydrogen or free electrons. The likelihood of excitation is thus higher in denser regions as it increases the probability of collisions. Therefore the [CII] line is thought to originate from dense gas clouds in the ISM. [CII] luminosity has also been observed to correlate with SFR in local galaxies [33]. There are a few interpretations of this correlation, the most common being that [CII] traces dense gas that stars will form out of. [CII] emission is more likely to originate from dense gas clouds, the same regions that will collapse to form new stars. It has been found as the major cooling mechanism, which allows the dense clouds to further cool and collapse. [82]. Another interpretation is that [CII] correlates with L_{IR}, and thus SFR [37]. Although the physical origins are not fully understood, [CII] provides a useful tool to study dense gas in the ISM.

The rotational transitions of carbon monoxide (CO) are a complimentary diagnostic of the ISM. The second most common molecule, behind only molecular hydrogen, CO emits in a set of rotational transitions. These produce CO(J,J-1) emission lines where J is the original rotational energy level and decay to the J-1 state emits a photon. The frequencies of the emitted photons follow $\nu_J = J \times 115$ GHz where J is the original rotational energy state of the CO molecule. CO molecules are excited to

higher J states by either ambient radiation or collisions. CO(5-4) and CO(4-3) are the most common transitions observed due to their relative brightness and their compatible frequency with current IR telescopes. Unlike [CII], the CO rotational lines trace molecular gas in the ISM. This is predominantly comprised of molecular hydrogen, H_2. This gas is not actively forming stars, but the reservoir that stars can form from in the future [16]. In dense gas clouds molecules are destroyed by UV radiation from young stars. The luminosity of the CO emission lines can be used to estimate total gas mass of a galaxy. [CII] and CO emission lines trace different phases of the ISM.

Observing emission lines allows astronomers to better characterize galaxies, not only through investigating the different phases of the ISM but also by indicating the galaxy's redshift. Since the rest frequency of emission lines is known, the redshift is easily measured. A spectral scan is used to search for the emission line to measure the observed frequency. Redshift is then easily calculated following Eqn. 1.1. This is a common and indisputable method to measure z. The width of the line in frequency space, σ, also called the velocity dispersion can be used to estimate the mass of the galaxy. Using the virial theorem, the average kinetic energy of particles is related to the average potential energy. The kinetic energy is proportional to the velocity dispersion squared, and the potential energy is proportional to the mass. This gives the following relation.

$$M_{\rm dyn} \propto \sigma^2 \tag{1.3}$$

Where $M_{\rm dyn}$ is known as the dynamical mass and σ is the velocity dispersion, measured from the width of the emission line. $M_{\rm dyn}$ is related to the halo mass, however the exact relation is complicated as it is based on a singular molecular or atomic species and its specific motions within the galaxy. It is still useful in estimating the mass scale. Observing emission lines allows further characterization of galaxies beyond specific chemical species.

1.2.3 Sub-millimetre galaxies

Sub-millimetre galaxies (SMGs) earned their name because they were originally observed at sub-millimetre wavelengths, often 870 μm. Ever since their study has moved far beyond this wavelength range [30]. SMGs are extremely bright in the IR driven by massive SFRs and large dust masses. The most luminous SMGs have measured SFRs greater than 2500 $M_{\odot}yr^{-1}$ and have been observed out to $z = 6$ with a mean redshift of 2.5 [84, 25]. The density of SMGs has been found to be much smaller than their less luminous counterparts [90]. This implies they are rare and extreme events. The discovery of SMGs at high redshift gives a window into extreme star formation in the early universe.

More distant galaxies, at a higher z, are more difficult to detect. The luminosity, L, is an intrinsic property of the galaxy however the flux, S, is what is measured and depends on a galaxy's distance from earth. Flux is a measure of how bright an object appears and is given by:

$$S = \frac{L}{4\pi D^2} \tag{1.4}$$

Where D is the distance from the galaxy to earth. Galaxies at high redshift are further away and therefore the flux we observe is lower causing them to be more difficult to detect. Observing in the sub-mm allows astronomers to observe galaxies at far greater distances than many other techniques, due to the shape of the IR SED. 870 μm is at a longer wavelength than the peak of the IR SED in the rest frame. When the galaxy is redshifted but still observed at 870 μm, the rest wavelength that is being traced is closer to the peak. The intrinsic luminosity from the galaxy at these shorter rest wavelengths is higher than at rest frame 870 μm. This compensates for the usual dimming due to distance described in Eqn. 1.4. SMGs are equally observable at $\lambda = 870$ μm between $z = 2 - 8$. This is shown in Figure 1.3 taken from Casey et al. (2014) [22]. It shows the flux of an example SMGs if it were to be observed at different wavelengths as a function of redshift. This figure confirms that for observed wavelengths between 850μm and 1.3mm, in the far IR, the observed flux is constant between $z = 2 - 8$. For shorter observed wavelengths, the observed flux continually

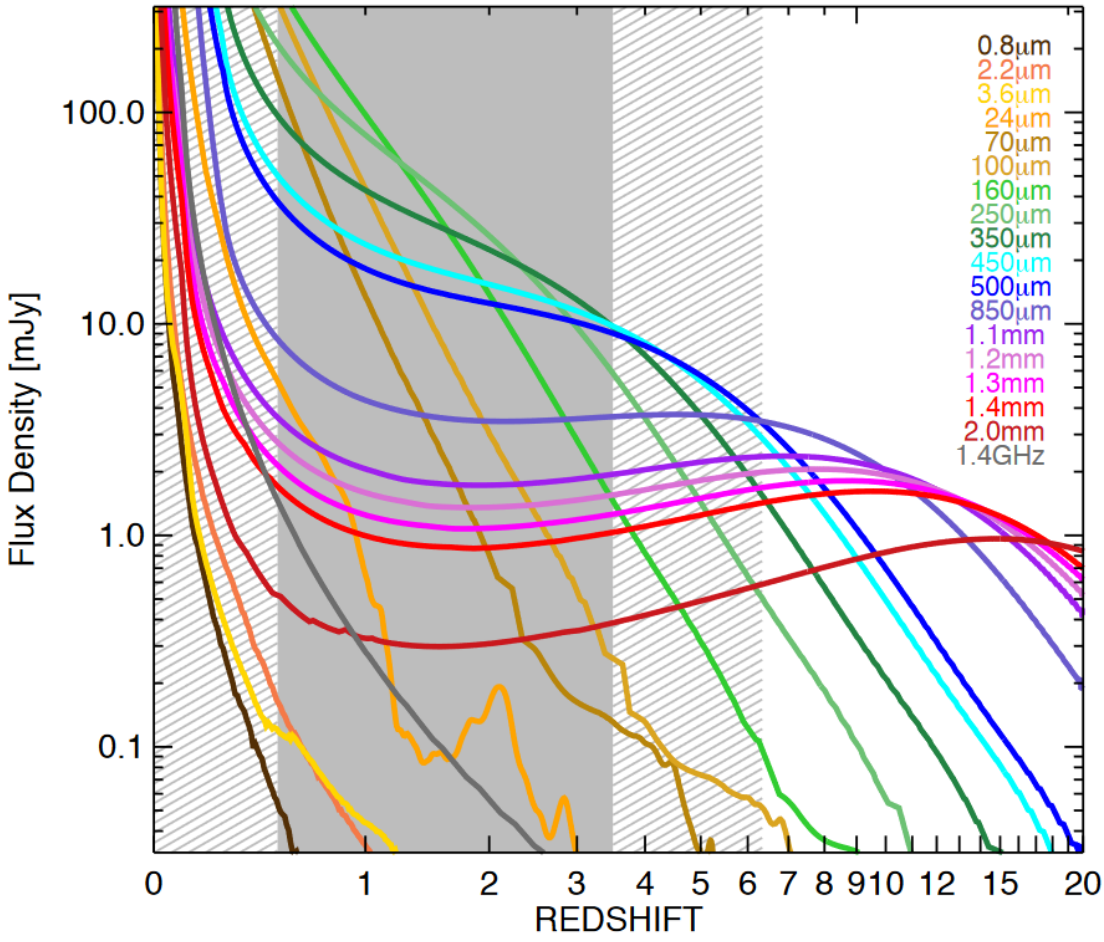

Figure 1.3: A figure, taken from Casey et al. (2014) [22], displaying the flux of an example SMG at different observed wavelengths and redshifts. At wavelengths in the Far IR (850μm $-$ 1.3 mm) the flux is seen to remain relatively constant between $z = 2 - 8$

drops. The K-correction of a galaxy is a measure of it's dimming due to redshift. Since SMGs do not dim, they are said to have a negative K-correction. This unique property of SMGs allows astronomers to investigate galaxy formation in the high redshift universe.

The discovery of SMGs changed the way astronomers think about galaxy formation at high redshift. The extreme SFRs place crucial constraints on galaxy formation models [101]. SMGs were thought to be the result of galaxy mergers producing a starburst, which drives the large amount of IR emission [93]. Since it is interaction

induced, this would imply SMGs are a short-lived phase of heightened SFR and L_{IR} in the evolution of some galaxies. Some recent studies have suggested that it is possible to replicate SMGs without a merger and sustain the large IR emission and SFR for an extended period [77]. Whatever their origin, they represent the largest SFRs observed at any redshift and create a laboratory to study the limits of star formation in galaxies.

SMGs present an opportunity to locate proto-clusters at high redshift. Their rarity is what makes them particularly useful [20]. Often proto-clusters are located by observing overdensities of galaxies; an excess of galaxies confined to a given volume. With more common galaxy populations it may be necessary to observe hundreds of proto-cluster members to ensure a statistical excess. With rare populations, like SMGs, only a few detections can lead to a significant overdensity. A group of five or more SMGs in close proximity is exceedingly rare so when observed, likely signifies a proto-cluster. However, the rarity of these populations also causes them to be more susceptible to Poisson noise leading to possible false detections [73]. It has also been suggested SMGs may play a critical role in the evolution of massive galaxies present at the center of clusters [103]. SMGs are a useful tool to observe and study proto-clusters in the early universe.

1.3 Simulating Galaxies

Astronomy is an observational science and it is often difficult to deduce the physical nature of observed correlations. To aid the interpretation of observations, theoretical models and simulations are needed. Through comparing models to observations, new insight is gained on the physical mechanisms which drive galaxies. Simulations and models must improve alongside observations. In the past few decades detailed hydrodynamic simulations of galaxies have improved to accurately reproduce and predict galaxy properties. For a galaxy simulation to be successful, it must accurately reproduce the three main components of galaxies: dark matter, gas, and stars.

Dark matter is comparatively the easiest of the three components to simulate. It

is modeled as collision-less and particles are only affected by the gravitational force. N-body dark matter simulations are initialized with N dark matter particles of a given mass and their evolution is governed solely by Newton's equation. In this vein, dark matter only are run on scales of $\gtrsim (500 \text{ Mpc})^3$ and have been very successful in predicting properties of the large-scale structure of the universe and the halos in which galaxies reside [83, 70]. Unfortunately, dark matter alone is insufficient to explain the dynamics of galaxies.

To simulate the ISM of galaxies, gas is modeled using the principles of fluid dynamics. This involves integrating the Euler equations which govern the movement of viscous fluids. This is often done in one of two ways: smoothed particle hydrodynamics (SPH) or mesh algorithms. In SPH the fluid itself is discretized and the movement of particles is calculated [97]. Whereas mesh methods involve discretizing space and then calculating the flow of fluid between cells. Mesh codes tend to be more accurate while handling discontinuities in pressure or density, however SPH codes are easily adaptable [96]. SPH also natively focuses more computing time on regions that are denser and therefore contain more particles. Mesh codes are traditionally restricted to the pre-defined mesh and therefore are not as adaptable. Adaptive or moving mesh algorithms have been implemented which alter the size of cells on the fly to overcome this problem. Both algorithms have been used to accurately reproduce observed properties of galaxies. On top of the method chosen, gas cooling rates are implemented from experimentally derived tables and forces from feedback and gravity are accounted for. SN enrich the surrounding gas with metals, which then diffuse around the galaxy. Gas dynamics in the ISM can be calculated using SPH or mesh algorithms modeling fluid dynamics.

Stars in simulated galaxies are born from dense gas. Typically there is a critical density (ρ_{crit}) set, above which gas is allowed to form stars. ρ_{crit} is usually on the order of 100 molecules cm^{-3}. Once this criterion is met, stars form at a rate governed by:

$$\dot{M}_* = \epsilon_* \frac{M_{\text{gas}}}{t_{\text{ff}}} \tag{1.5}$$

Where $\dot{M}_*$ is the rate that stars form at and can be thought of as the 'instantaneous' SFR. t_{ff} is the local free fall time, which is given by the Jeans equation as $\sim \sqrt{\frac{1}{G\rho_{\rm gas}}}$ [57]. ϵ_* is the star formation efficiency. This is typically set at a few percent to match observed relationships between gas and SFR surface density. This relationship is known as the Kennicutt-Schimdt law and a common interpretation is that star formation is inherently inefficient [61]. The nature of ϵ_* and the interpretation of the relatively low value found is uncertain [64]. This rate then defines a probability and gas particles are stochastically turned into star particles. Stars form in simulated galaxies using this simple prescription however, the difficulty is modeling how young stars interact with the ISM through stellar feedback.

The intrinsic problem is that stellar feedback occurs on small scales ($\ll$ 100 pc) while the dynamics of the entire galaxy must still be simulated on large scales ($>$ 10 kpc). Somehow simulations must cover this large dynamic range. The compromise that is often taken involves using 'sub-grid' models [92]. These are phenomenological models that simulate feedback as a momentum and/or thermal energy 'kick' by artificially increasing the momentum or temperature of surrounding gas particles. The strength of these 'kicks' is based on the physical properties of the star particles but can be tuned to match observed properties of galaxies. Additional momentum or pressure caused by the increased temperature causes disruption in the birth clouds that stars are born in. On a larger scale, this affects the dynamics of the galaxy and can even drive outflows. Including 'sub-grid' models allows the simulations to replicate the physics of stellar feedback while still simulating the dynamics of the entire galaxy.

In general, recent hydrodynamical simulations have been successful in reproducing observed properties of galaxies. Distributions of stellar masses and even the star forming main-sequence (SFR - M_* relationship) and many other observations have been reproduced [110, 67]. The key word here being reproduced, as these simulations are not predictive in nature. Given the tunable parameters such as the star formation efficiency and the strength of feedback, these simulations are in a sense designed to

match observations. This concern is can be addressed using small scale simulations. Results from isolated simulations of stellar feedback or star formation can guide the implementation of phenomenological models. This partnership between small and large scale simulations will decrease the dependence on observations and lead to more predictive models. These simulations are still incredibly useful in interpreting observations of galaxies and have given numerous insights into galaxy formation.

In contrast to detailed hydrodynamical simulations, abundance matching is a statistical method that is commonly used to model properties of galaxies. This is a semi-analytic approach built upon dark matter only simulations that aims to connect galaxy properties to dark matter halos. In its first and simplest form, the goal was to investigate the M_* - M_{halo} relation. By comparing the distribution of halo masses from dark matter only simulations to observed distributions of stellar mass, a mapping from one to the other is inferred [107]. In recent years models have become increasingly complex, attempting to match a multitude of observations including the cosmic SFRD, stellar mass distribution and SFR distributions [75, 2]. Abundance matching is an incredibly powerful method as it allows galaxy properties to be assigned to dark matter halos in N-body simulations. Numerous applications can stem from this in attempting to interpret observations or predict the outcome of future surveys. The common criticism of abundance matching is that it does not provide physical insight since it is simply a method to connect observations to dark matter only simulations. Yet no one can deny the usefulness of semi-analytic or phenomenological models like abundance matching in its wide range of applicability.

1.3.1 Feedback In Realistic Environments (FIRE) Simulations

The feedback in realistic environments (FIRE) simulation suite is a set of hydrodynamical galaxy simulations developed by Phil Hopkins [49]. These simulations aim to accurately model stellar feedback and simulate the evolution of galaxies. They simulate the halo along with all the necessary baryonic physics. The main innovation is

the explicit implementation of stellar feedback. Feedback from 3 main channels is included: Radiation pressure, SN, stellar winds. In this manner, the FIRE simulations are more predictive then previous generations. From stellar feedback alone, many of the observed relationships are produced. The FIRE simulations have provided great insight into how small scale stellar feedback can affect large scale galaxy dynamics.

Three channels of stellar feedback are included in the FIRE simulations: radiation pressure, SN explosions and stellar winds. In a set of studies these channels were modeled, implemented and tested [53, 52]. All three channels are implemented as a momentum or thermal energy (temperature increase) boost to surrounding gas particles based on a star particle's physical properties. Unlike previous 'sub-grid' models, these are modeled from first principles and their strength is not tuned to match observations. Radiation pressure is applied as momentum to surrounding gas particles based on the luminosity of a given star particle. The rate of SN is tabulated based on a star particle's age and metallicity. This defines a probability per unit time and SN explosions are then triggered stochastically. When triggered, thermal energy and momentum are injected into surrounding gas particles creating a supersonic blast wave. When resolved this is propagated outward naturally under the SPH framework. In low density regions when the blast wave is not resolved, work done by thermal energy is accounted for by converting it to momentum. Stellar winds inject momentum and mass into surrounding gas particles, the amount of which is calculated based on a star particle's age and metallicity. No one feedback channel is sufficient and all channels are necessary to regulate star formation.

The FIRE simulations put stellar feedback in the context of cosmological evolution. The full scale of the dark matter halo is simulated concurrently with the gas and stars. The scale of the simulated box is often $\sim$ 500 kpc. A version of SPH, known as P-SPH [50] is used to calculate the gas dynamics. This version formulates the equations of motion in terms of pressure and entropy. P-SPH preforms better in fluid mixing problems and at discontinuities compared to canonical density-energy or density-entropy versions of SPH. Stars form from gas only if it is dense and locally

self gravitating. This is a slightly more stringent criterion then the density alone as it also involves evaluating the velocity of the gas particles. However, stars form with 100% efficiently per free-fall time, i.e. the star formation efficiency $\epsilon_* = 1$. This is starkly different than previous generations of simulations which assume $\epsilon_* \sim 0.03$ to match the Kennicutt-Schmidt law.

Even though the FIRE simulations allow star formation to happen with 100% efficiency, the Kennicutt-Schmidt law is still produced [80]. Star formation is not naturally inefficient but is regulated by stellar feedback. On small scales stars form and then disrupt the gas clouds they were born in. On large scales, this manifests as the Kennicutt-Schmidt relation between gas and SFR surface density. Incredibly, it is predicted simply from stellar feedback. It is often argued that the details of stellar feedback are unimportant because on cosmological timescales, as it is not the rate limiting step. What controls star formation is instead attributed to accretion of gas into the halo and galaxy. The FIRE simulations have displayed the importance of stellar feedback in the cosmological evolution of galaxies.

Chapter 2

Star Formation Rate Indicators in the FIRE simulations

2.1 Introduction

The total infrared luminosity (L_{IR}) is one of the most widely used SFR indicators. For decades, it has been used to estimate SFR for a diverse set of galaxies spanning all epochs. It offers a distinct advantage of many SFR indicators that it is not affected by dust attenuation [59]. At lower wavelengths, indicators such as the UV luminosity must account for the effects of dust obscuration which introduces an inherit uncertainty. Whereas in the IR, dust does not significantly obscure light, however a L_{IR} to SFR conversion does contain its on set of caveats.

The main issue is believed to be dust heating from old stars. This will cause L_{IR} to overestimate the SFR as the K98 conversion factor assumes they do not contribute. Observationally, many studies have found dust heating from old stars to be non-negligible [76, 62, 5]. This may be a systemic issue when using the IR luminosity to trace SFR. By comparing the IR luminosity to more sophisticated SFR indicators, recent studies have shown the it tends to overestimate SFR, especially at low SFRs [106, 104]. Some studies have also suggested that the star formation history (SFH) of a galaxy may introduce further uncertainty [45]. In the original work K98 states that the L_{IR} is only a valid tracer of SFR under certain conditions, nevertheless it is still routinely applied to many diverse galaxy populations.

In this study, we develop a simple radiative transfer model to estimate L_{IR} of simulated galaxies based on dust absorption. This model is then applied to the FIRE simulation suite with the goal of testing the simple linear L_{IR}-SFR conversion based on the K98 model. The FIRE simulations present great opportunity to forward model observations as they are more predictive than previous generations of simulations.

Section §2.2 describes the radiative transfer model and the FIRE simulations used. The results when the algorithm is applied to the FIRE simulations is shown in §2.3. In §2.4 we discuss our results and some of the implications.

2.2 Methods

2.2.1 Radiative Transfer Model

The goal of developing this method is to estimate L_{IR} from post-processing the FIRE simulations using a simple, fast and flexible radiative transfer model. The basic premise is to estimate the spectrum of each star particle in the simulation and the column density of dust between that star particle and the edge of the simulation. Combing these measurements and using the radiative transfer equation, the amount of light originating from each star particle that is absorbed by dust is calculated. This is its contribution to L_{IR}. This procedure allows us to separate contributions from different star particles; specifically differentiating between the old and young stellar populations. As stated in the Introduction, previous studies have suggested that this is likely a cause of L_{IR} overestimating SFR.

Py-FSPS, a python wrapper of the original flexible stellar population synthesis package [40, 28] is used to estimate the spectra for each star particle. It is calculated based on each star particles age and metallicity. This package begins with pre-calculated stellar spectra templates spanning many ages, metallicities and masses. When age and metallicity are specified it convolves the spectra of different mass stars with the observed distribution of stellar masses (Stellar IMF) to output a spectrum for the stellar population. A Chabrier [23] IMF is used. Using Py-FSPS spectra for each star particle is calculated based on it's age and metallicity. This is used as the intrinsic or bolometric luminosity (L_{bol}) for each star particle.

The column density of dust between each star particle and the edge of the simulation is calculated by integrating the gas density along a given line of sight. The code used to preform this calculation was originally written by Hopkins et al. (2005) [51] and is adapted for this study. Beginning at the source, steps of length $\frac{1}{2}h_{smooth}$ are

taken along a given direction. h_{smooth} can be thought of as the resolution of particles in SPH and is variable; it will be smaller, and therefore more integration steps will be taken, in regions which are more dense. The gas density and metallicity are integrated along the given direction until the edge of the simulation volume. This integration yields the column density of gas, n_H, and the column metallicity, n_Z along the given line of sight. From these the column density of dust (n_{dust}) is calculated assuming a constant dust to metals ratio (f_{dtm}) of 0.4 [36, 55]. This calculation is summarized below:

$$n_{dust} = f_{dtm} \times n_Z \times n_H \tag{2.1}$$

Once the column density and the spectra of the stellar population are known, the

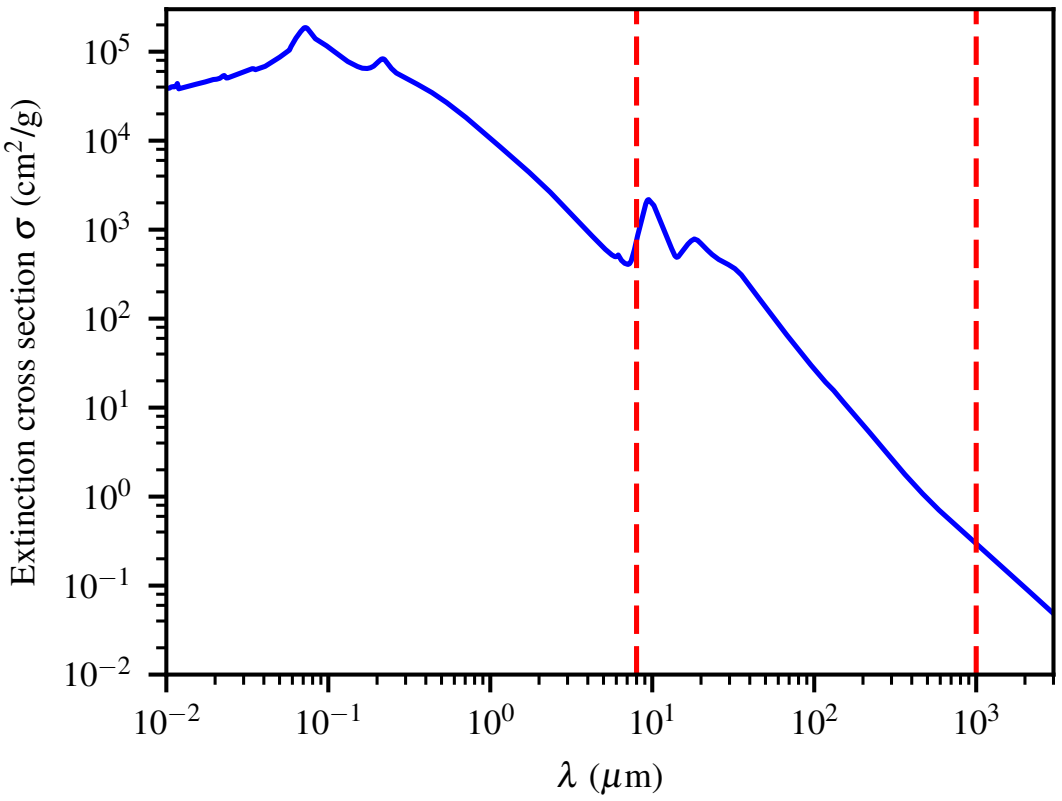

Figure 2.1: The extinction spectra of dust used in the radiative transfer calculation is shown. This is taken from Weingartner & Draine (2000)[112]. The two red lines display the IR region of the spectrum. In this region, the extinction cross section is much lower than in the UV-visible region at $\lambda < 1$ μm.

extinction properties of dust are needed to calculate absorption. The extinction cross section (σ_λ) of dust in the ISM is taken from Weingartner & Draine (2000)[112]. This is based on a study of stellar spectra within the milky way and is shown in Figure 2.1. Extinction is the strongest in the visible and UV regions of the spectrum at $\lambda < 1\mu$m. There is significantly less extinction at $\lambda > 10\mu$m, in the IR region of the spectrum. For use in this study we normalize to the amount of metals by multiplying the extinction cross section by the dust to gas ratio along the line of sight ($\mathrm{f_{dtg}} = \mathrm{f_{dtm}} \times n_Z$) to that observed in the milky way ($f_{\mathrm{dtg,MW}} = \frac{1}{123.6}$). The optical depth ($\tau$) is calculated as shown below.

$$\tau_\lambda = \frac{\mathrm{f_{dtg}}}{\mathrm{f_{dtg,MW}}} \times n_{\mathrm{dust}} \times \sigma_\lambda \tag{2.2}$$

From here we use the radiative transfer equation and a simple numerical integral to calculate the absorbed luminosity ($\mathrm{L_{abs}}$)

$$\mathrm{L_{abs}} = \int (1 - e^{-\tau_\lambda}) \mathrm{L_{bol,\lambda}} \, d\lambda \tag{2.3}$$

The result is the total power absorbed along the chosen direction to calculate n_{dust}. There may be complex dust geometries within the galaxy causing n_{dust} to vary wildly as a function of direction. Choosing only one direction to calculate n_{dust} is insufficient to accurately estimate the average value. To accurately estimate the line of sight properties the above calculation must be preformed for some number of directions and the results averaged. Figure 2.2 displays the convergence of $\mathrm{L_{abs}}$ as a function of the number of lines of sight averaged. The direction of each line of sight is randomly sampled uniformly from $\theta \in (0, \pi)$ and $\phi \in (0, 2\pi)$. The average fractional difference is calculated by comparing to $\mathrm{L_{abs}}$ calculated using a given number of lines of sight to 1000 lines of sight using the equation below.

$$\text{Average fractional difference} = \left\langle \left| \frac{\mathrm{L_{abs,1000}} - \mathrm{L_{abs,}}X}{\mathrm{L_{abs,1000}}} \right| \right\rangle_{\text{particles}} \times 100\% \tag{2.4}$$

Where X is the given number of lines of sight averaged. The data shown in Fig. 2.2 is taken from the M11 simulation at $z = 0$ (See §2.2.2 for details). Below 10 lines of sight the average fractional difference is large but drops rapidly to approximately 10% at 15 lines of sight. Above 15, averaging more lines of sight provides diminishing returns at the average fractional difference slowly decrease to 5% and below when one hundred or more lines of sight are averaged. 15 lines of sight to average is used when preforming this calculation unless otherwise specified. This is chosen to obtain 10% accuracy while limiting the amount of computational resources needed. It is worth note that this figure displays the scatter for individual star particles and since galaxies in the simulations often contain $> 10^4$ star particles this uncertainty is dampened.

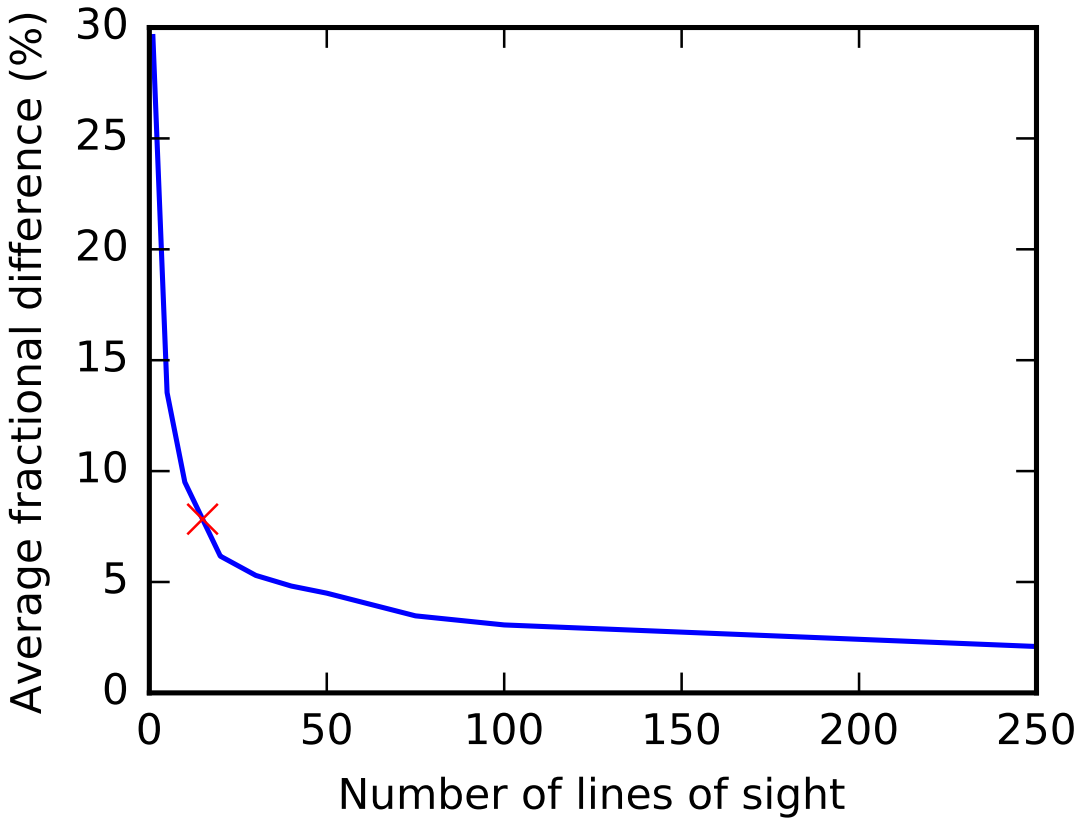

Figure 2.2: A convergence test that show the average fractional difference between $L_{abs}$for a given number of lines of sight used compared to 1000. 15 lines is displayed by the red cross. This is chosen for any further calculation because it achieves less than 10% error while limiting computational resources needed.

The result is the luminosity absorbed that originated from a given star particle. Under the assumption that the dust is in thermal equilibrium, the total power absorbed must also be re-emitted. Dust in the ISM of galaxies is known to be between 30K to 50K, therefore the blackbody will peak between 60 μm to 90 μm and greater than 99% of the thermal emission will occur in the IR region of the spectrum [22]. Thus, it is safe to assume the total power absorbed will be re-emitted in the IR. Since the dust itself does not absorb IR light, as shown by the low extinction cross section in Fig. 2.1, IR light will travel unimpeded out of the galaxy. With these properties combined, the contribution to the infrared luminosity from a star particle is calculated as the average L_{abs} over 15 lines of sight: $L_{IR,particle} = \langle L_{abs} \rangle_{directions}$.

To calculate the total L_{IR} of a simulated galaxy, the algorithm described above is repeated for each star particle and the sum is taken. Star particles within $\frac{1}{10}R_{Vir}$ of the centre of the halo are considered part of the galaxy. Similarly, only gas particles within $\frac{1}{2}R_{Vir}$ are considered when calculating n_{dust}. At this radius the gas density drops to where it's contribution to n_H would be negligible. It is also uncertain whether hot gas in the halo can sustain dust grains [35]. A flowchart outlining the algorithm used to calculate L_{IR} from a simulated galaxy is shown in Fig. 2.3.

2.2.2 Simulation Sample

In this study we use the standard FIRE (SF) simulations suite described in Hopkins et al. (2014) [49] and the massive F.I.R.E. simulation suite (MF) described in Feldmann et al. (2016) [38]. Both suites use P-SPH to model the evolution of the gas and the exact same stellar feedback implementation. There are slight differences in the mass resolutions: SF ranges from 5×10^3 $M_\odot$ to 2.6×10^5 $M_\odot$ for baryons and 2.5×10^4 $M_\odot$ to 1.5×10^6 $M_\odot$for dark matter, where as MF uses 3×10^4 $M_\odot$ for baryons and 1.7×10^5 $M_\odot$ for dark matter. The main difference is the halo mass of galaxies simulated. SF contains galaxies with halo mass ranging from 10^{11} $M_\odot$ to 10^{13} $M_\odot$ at $z = 0$. MF, hence the name, simulated larger galaxies with $z = 0$ halo masses of $\sim 10^{14}$ $M_\odot$.

For each suite, several snapshots are analyzed. These span almost the entire age

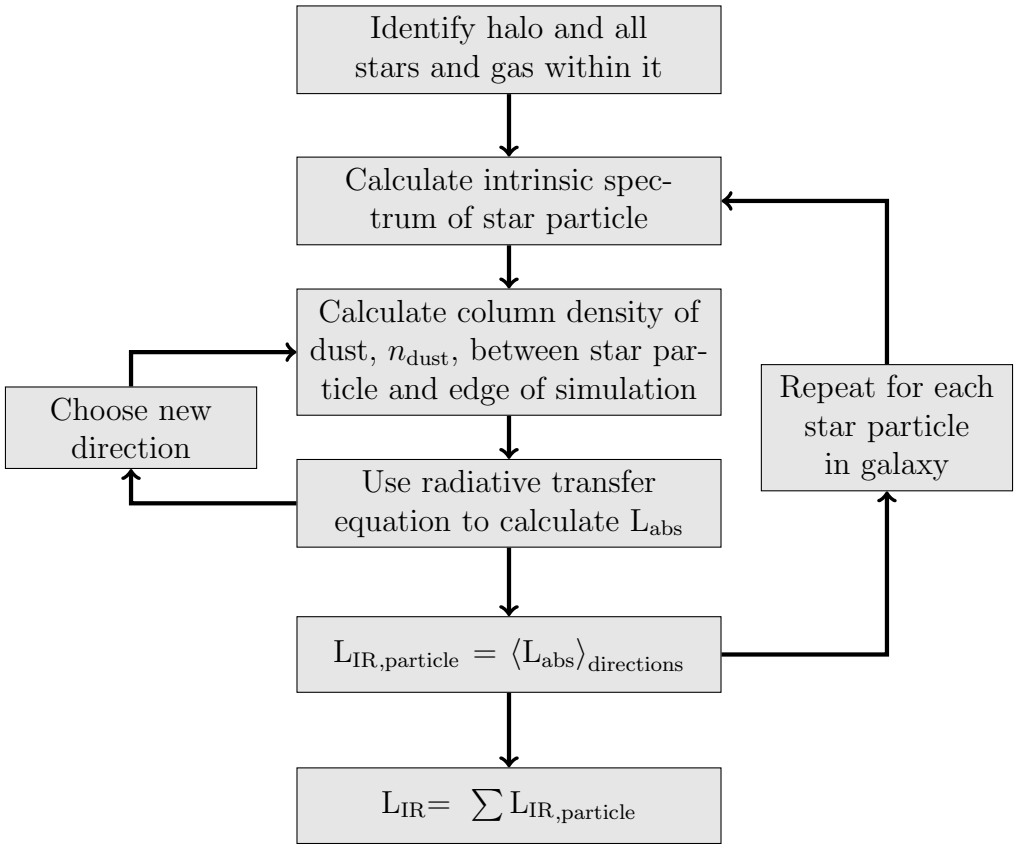

Figure 2.3: An overview of the algorithm described in § 2.2 is shown.

of the universe and encompass all phases of galaxy evolution. For SF, snapshots at $z =$ 3, 2.2, 1.4, 0.8 and 0 are used. MF includes snapshots at $z = 6$, 5, 4, 3, 2.2, 2.1 and 2. The MF suite terminates its simulations at redshift two. This is because FIRE does not include the physics of AGN. AGN are known to exist ubiquitously in massive galaxies at $z < 2$ [39]. Like stellar feedback, AGN imparts energy and momentum onto the gas in the galaxy which prohibits it from forming stars [6]. Galaxies with AGN have essentially no star formation activity. Since this is not included, MF would over predict the stellar mass of massive galaxies at low redshift. SF simulates less massive galaxies, not known to host AGN, thus is not prone to this weakness. The simulations contain the main halo and often several sub-halos. These are less massive halos that exist within the volume of the simulation. For each snapshot, there is a catalog of dark matter halos are identified within the volume. To avoid analyzing spurious halos, only halos containing more than 2000 star particles are analyzed. This

criterion ensures each halo analyzed contains a galaxy.

2.3 Results

Figure 2.4 displays the SFR_{100Myr} vs. L_{IR} of all galaxies analyzed. SFR_{100Myr} is the 100 Myr averaged star formation and is calculated by summing the mass of all star particles with age less than 100 Myr and dividing by 100 Myr. This timescale is consistent with the age of stars that the IR luminosity traces. Unless otherwise specified, whenever SFR or SFR_{true} is used this implies SFR_{100Myr}. Any galaxy that is found to have $L_{IR} < 10^{-5}\ L_{\odot}$ or $SFR_{100Myr} = 0$ is not considered for this analysis. Also displayed is the moving average of L_{IR} as a function of SFR along with the SFR to L_{IR} conversion following from the K98 model. For consistency, we derive a conversion factor based on the Py-FSPS package and Chabrier IMF used to calculate L_{IR}. The luminosity for a stellar population with age of 100 Myr and a constant star formation history is calculated and the conversion factor is found to be $1.66 \times 10^{-10} \frac{M_{\odot} yr^{-1}}{L_{\odot}}$. This is within the range of conversion factors used in other studies and allows for self-consistency of ours [58, 59].

At first glance, our results shown in Fig. 2.4 broadly agree with the K98 model. As SFR increases, L_{IR} also increases in an approximately linear relationship. However, upon closer inspection, there are two main difference between our data and the K98 model: The moving medians are generally at a higher L_{IR} then the K98 model at a given SFR and there is a large amount of scatter in L_{IR} at a given SFR. These two differences will be discussed and highlighted in the following paragraphs and figures.

The difference between the simulated sample and the K98 model is not uniform. When binned in SFR, the moving median agrees well at high SFR but begins to diverge at SFR $< 1\ M_{\odot} yr^{-1}$. The moving median lies above the K98 model in the low SFR regime. The opposite behavior is observed when the sample is binned in L_{IR}. The sample and K98 model agree at $L_{IR} < 10^{9}\ L_{\odot}$ but the moving median lies higher than the model at larger luminosities. If a galaxy lies at a higher L_{IR} then what is predicted by the K98 model, this implies the K98 model is over predicting the

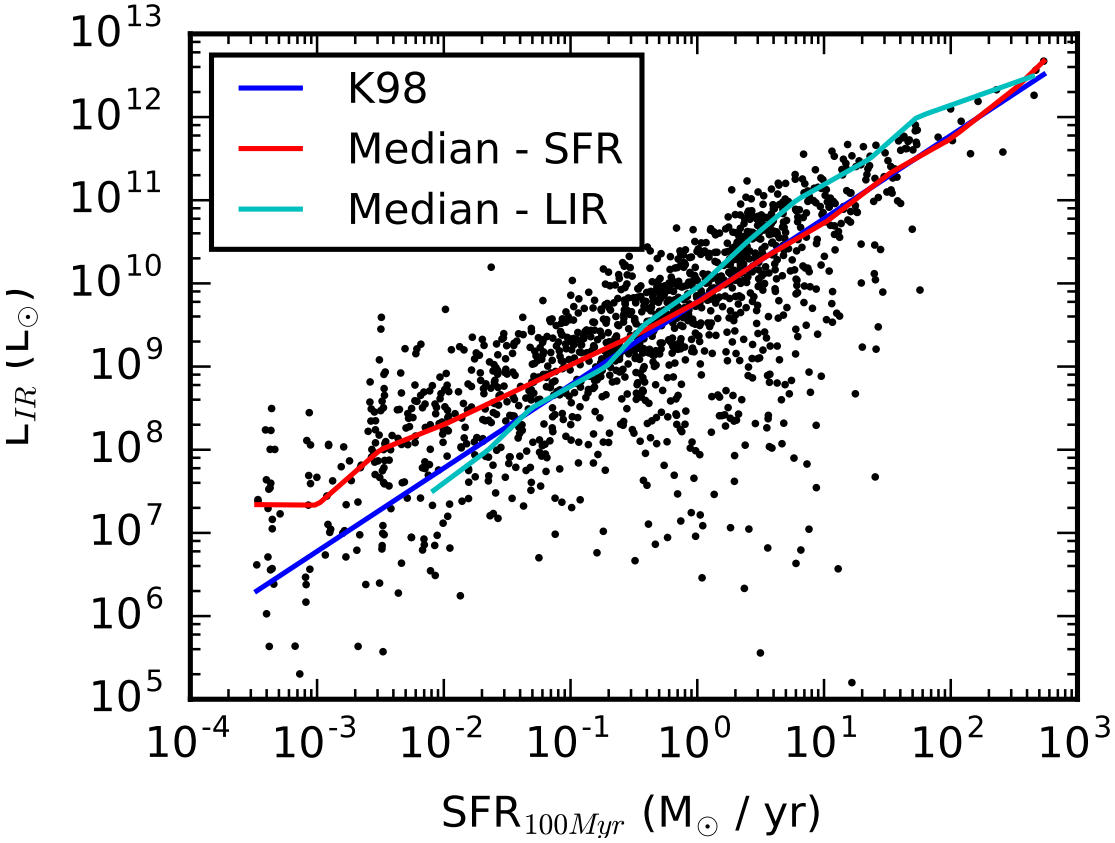

Figure 2.4: SFR vs L_{IR} for is shown for the entire sample of simulated galaxies. The K98 conversion, the moving median of our sample as a function of SFR and $L_{IR}$is also displayed. When binned in L_{IR} or SFR the median does not always agree but in general they tend to lie above the K98 line.

SFR. The simple linear conversion from the K98 model produces a higher SFR than the true SFR of a galaxy. The SFR of a galaxy calculated from the K98 model will be referred to as SFR_{IR} and is calculated simply as $SFR_{IR} = K98 \times L_{IR}$. To compare this to the true SFR, the SFR residual (SFR_{Res}) is defined as:

$$\text{SFR residual} = SFR_{Res} = \frac{SFR_{IR}}{SFR_{True}} \tag{2.5}$$

For the moving average shown in Fig. 2.4, since it consistently lies above the K98 model, SFR_{IR} is larger than SFR_{True}, and the $SFR_{Res}$of our sample will on average be greater than one. This implies the simple linear conversion implied by the K98 model on average overestimates the SFR of galaxies.

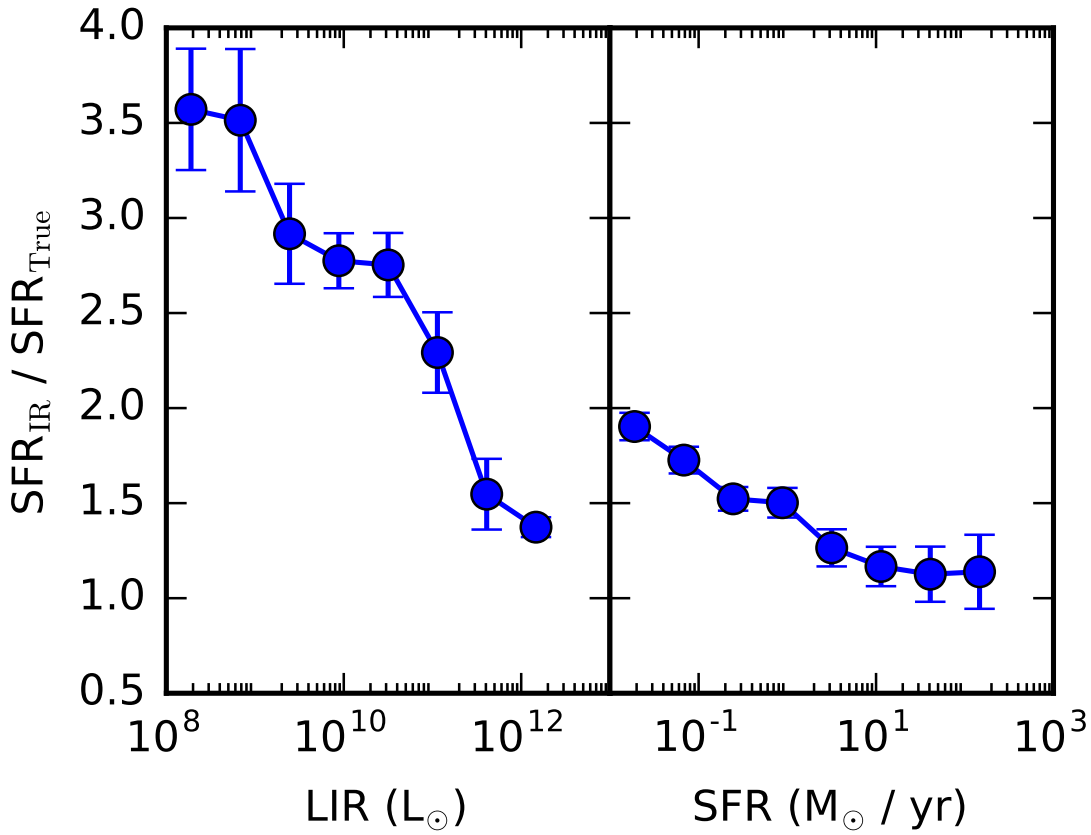

Figure 2.5: The figure displays the mean SFR_{Res} as a function of L_{IR} and SFR. The error bars represent the standard error of the sample in each bin. SFR_{Res} decreases as both quantities increase, however it peaks higher when the galaxy sample is binned in L_{IR}

Figure 2.5 shows the average SFR residual in SFR and L_{IR} bins. The error bars represent the standard error in each bin. The right panel displays at low SFR the SFR residual is at its highest at approximately two and then decreases as SFR increase until SFR = 10 $M_{\odot}yr^{-1}$. At SFR > 50 $M_{\odot}yr^{-1}$ the SFR residual is consistent with one. This behavior mirrors what is seen in Fig. 2.4. The left panel shows similar behavior of the SFR residual when galaxies are binned instead in L_{IR}. At $L_{IR} < 10^9$ $L_{\odot}$ the SFR residual is at it's largest, approximately 3.5. It then monotonically decreases as L_{IR} increases to reach just below 1.5 at $L_{IR} > 10^{12}$ $L_{\odot}$. Unlike when binned in SFR, the SFR residual is always larger than one when it is binned in L_{IR}. It is worth note that there are only 6 galaxies in the sample with $L_{IR} > 10^{12}$ $L_{\odot}$. A larger sample is

necessary to draw meaningful conclusions about this extremely bright population.

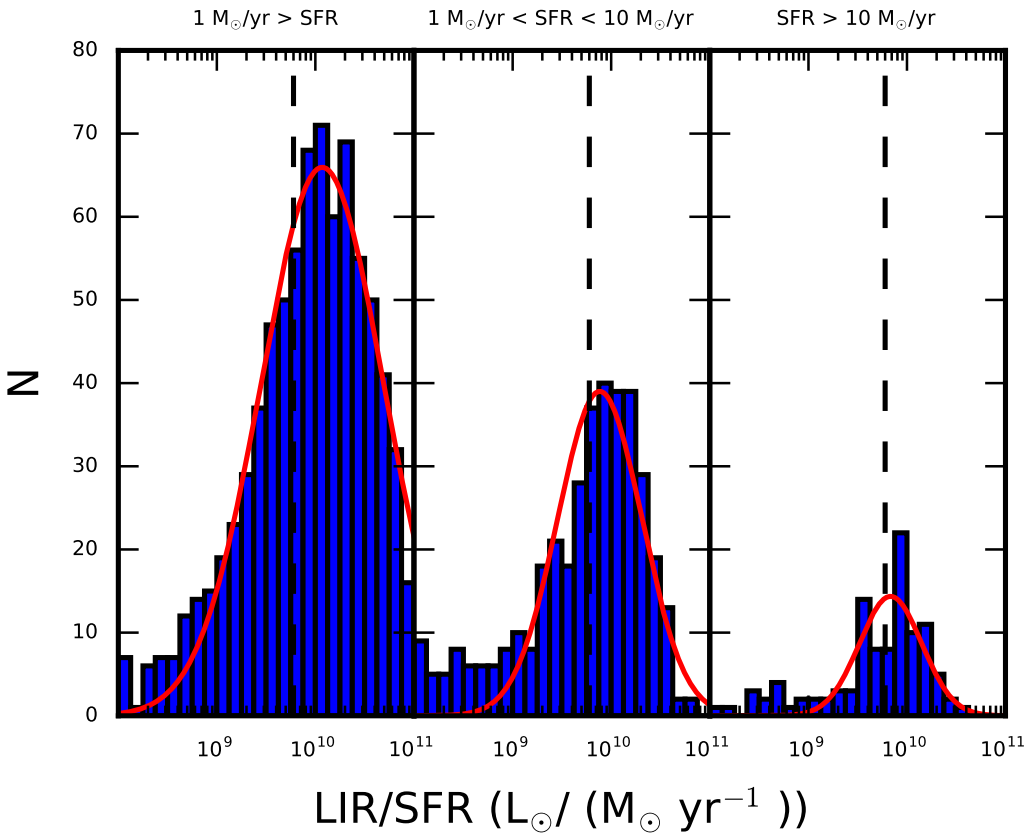

Figure 2.6: The distribution of L_{IR}/SFR for the simulated sample in three different SFR bins is shown. The red line displays a log-normal fit to each distribution and the black dotted like is the inverse of the K98 conversion factor used Each distribution is well fit by a log-normal except for a long tail at low L_{IR}/SFR.

Along with the over estimation of SFR_{true}, there is substantial scatter of our sample at a given L_{IR} or SFR. To quantify this figure 2.6 shows the distribution of L_{IR}/SFR in low, medium and high SFR regimes. A log-normal fit to each distribution is also shown. The magnitude of the scatter is the smallest in the high SFR regime at 0.31 dex. This increases to 0.42 and 0.62 in the medium and low SFR regime respectively. A log-normal distribution is shown to provide a good fit in all three regimes however, there is a tail to low L_{IR}/SFR values. This is most evident in the medium SFR regime. This population of galaxies is visible in Fig. 2.4 with SFR between 1 $M_\odot yr^{-1}$ and 10 $M_\odot yr^{-1}$ with $L_{IR} < 10^8$ $L_\odot$. This is up to three orders of

magnitude lower than what is expected from the K98 model and the sample mean.

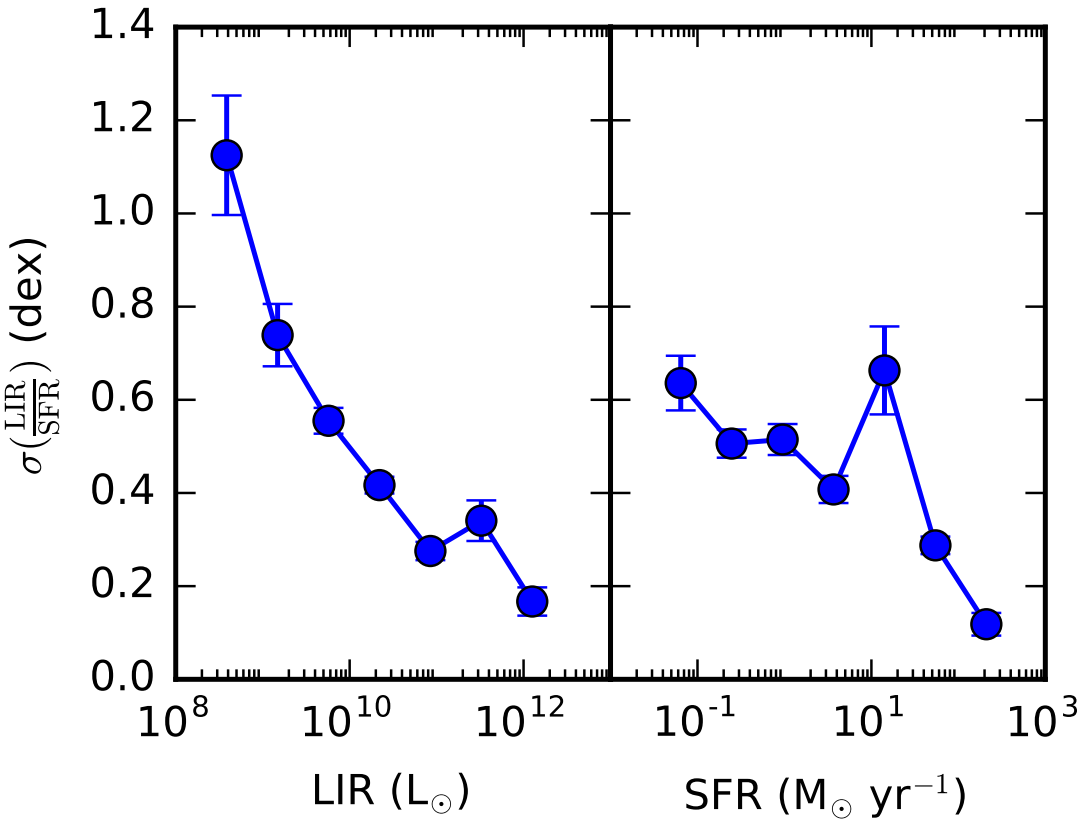

Figure 2.7: The scatter in the distribution of L_{IR}/SFR is shown as a function of L_{IR} and SFR. This is the logarithmic scatter and is shown in orders of magnitude (dex). This is found by fitting log-normal distributions to each distribution. The error bars represent the error in this least-squares fit.

The one sigma standard deviation of L_{IR}/SFR ($\sigma\left(\frac{L_{IR}}{SFR}\right)$) over a range of SFR and L_{IR} bins is shown in Figure 2.7. This is the logarithmic scatter and is calculated by fitting a log-normal function to the L_{IR}/SFR distribution in each bin, similar to what is displayed in Fig. 2.6. Both curves generally decrease with increasing SFR or L_{IR}, although there is a strong spike at SFR ~ 10 $M_\odot yr^{-1}$ and a less pronounced peak at $L_{IR} \sim 5 \times 10^{11}$ $L_\odot$. $\sigma\left(\frac{L_{IR}}{SFR}\right)$ is lowest in the brightest and most actively star forming population at < 0.2 dex. When binned in L_{IR}, it peaks at a standard deviation of ~ 1.1 dex compared to 0.6 when the sample is binned in SFR.

To further understand the physical origin of the behavior of L_{IR}/SFR, we investigate the contribution of old and young stellar populations to L_{IR}. The contribution to L_{IR} from young stars, defined by age < 100 Myr, will be labeled $L_{IR,young}$ and similarly $L_{IR,old}$ the contribution of stars older than 100 Myr. This is not the direct light observed from these populations but the power emitted by them that is absorbed by dust in the ISM and re-emitted. The K98 model assumes that only young stars contribute to L_{IR}. In this simple model, by the times stars are old, their birth cloud is disrupted and there is a negligible dust column density. Thus the true SFR can be calculated as: $SFR_{true} = K98 \times L_{IR,young}$. From this we can define a simple model to formulate SFR_{Res} in terms of $L_{IR,young}$ from Eq. 2.5.

$$SFR_{Res} = \frac{SFR_{IR}}{SFR_{true}} = \frac{K98 \times L_{IR}}{K98 \times L_{IR,young}} = \left(\frac{L_{IR,young}}{L_{IR}}\right)^{-1} \tag{2.6}$$

This equation relates SFR_{Res} to $\frac{L_{IR,young}}{L_{IR}}$; the fractional contribution to L_{IR} from young stars or the young fraction. With the algorithm used, we can separate the contribution from old and young stars. If the main mechanism causing SFR_{IR} to overestimate the true SFR is the contribution of old stars, the SFR_{Res} of our sample should follow the relationship stated in Eqn. 2.6. In figure 2.8 SFR_{Res} is plotted against the L_{IR} young fraction for the sample of simulated galaxies along with the simple model derived above. There is a weak negative correlation of SFR_{Res} with L_{IR} young fraction. This signifies that when old stars contribute more to L_{IR}, SFR_{IR} overestimates the true SFR by a larger amount. Yet, the data does not agree well with the simple model we have derived. Especially at low young fraction, the model overestimates the data by two orders of magnitude. The model and mean of the sample agree relatively well when the young fraction approaches one but there is a large spread in SFR_{Res} values. This significant scatter at a fixed L_{IR} young fraction implies there is another mechanism affecting the behavior of SFR_{Res}.

To investigate the discrepancy between the data and model shown in Fig. 2.8 we

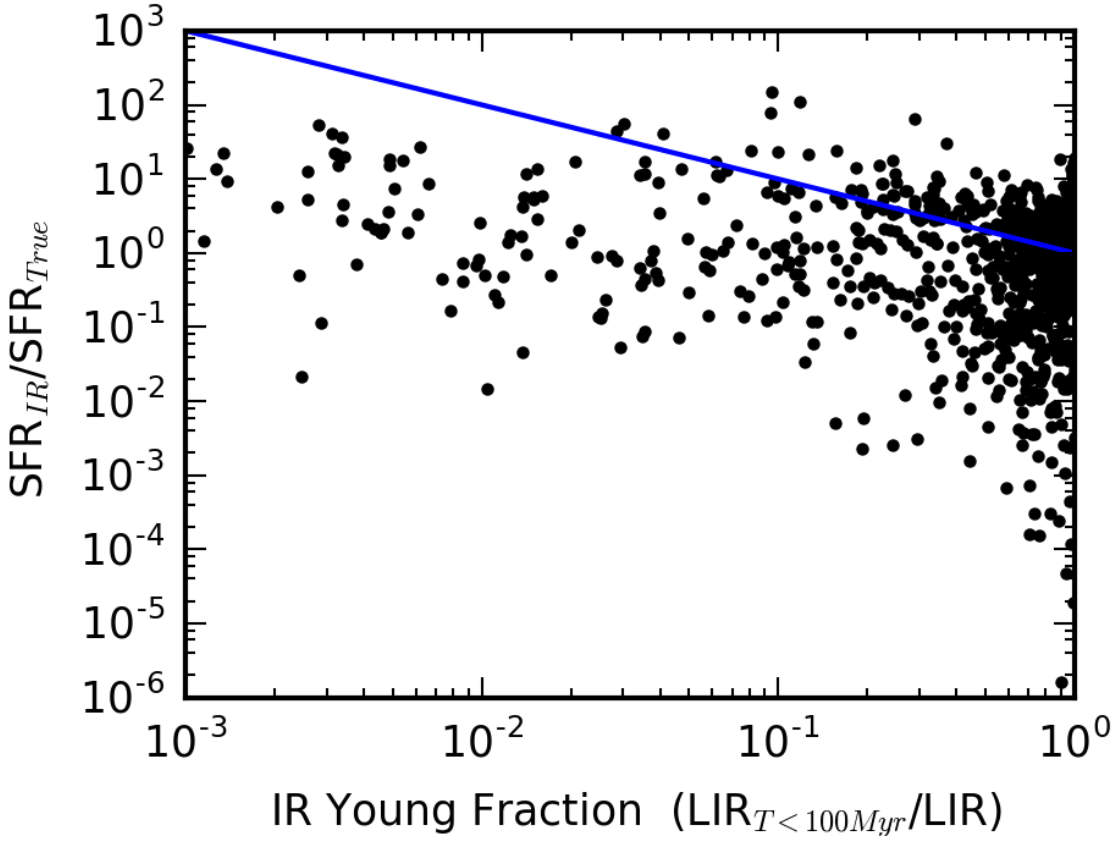

Figure 2.8: SFR_{Res} is plotted against the fractional contribution of young stars to the IR luminosity. The simple model described in Eqn.2.6 is also displayed. Although there is a weak negative correlation between SFR_{Res} and the young fraction, our simple model does not explain what is observed.

define the young fraction residual (YF_{res}):

$$YF_{res} = \frac{SFR_{Res}}{(\text{young fraction})^{-1}} \tag{2.7}$$

This is the discrepancy between the actual SFR_{Res} and that predicted by Eqn. 2.6 based on the young fraction. This metric quantifies the discrepancy between the K98 model considering the contribution of old stars and what is observed. In figure 2.9 we plot YF_{res} versus two physical quantities of the simulated galaxies: the absorbed fraction and the slope of the star formation history (SFH α). The absorbed fraction (f_{abs}) is the fraction of the intrinsic luminosity of stars that is absorbed and is calculated simply as L_{IR}/L_{bol}. To asses the behavior of the recent star formation

history, we re-bin the SFR into four 25 Myr wide bins spanning the previous 100 Myr before the snapshot. If no stars have formed in a given time bin, the SFR is set to 10^{-6} $M_{\odot}yr^{-1}$and galaxies that contain zero star formation in two or more time bins are not analyzed. We then fit a simple power law of the from SFR $\propto t^{\alpha}$. A positive SFH α implies the SFR of a given galaxy has been rising for the previous 100 Myr prior to the snapshot. Similarly, a negative SFH α implies the SFR of the galaxy has been recently declining. This measure contains no information about the long-term evolution of the galaxy only the most recent 100 Myr.

Figure 2.9 displays a very tight positive correlation between YF_{res} and f_{abs} at low values of f_{abs} ($< 10^{-1}$). At higher values, there is still a reasonable correlation between the two variables but a considerably larger amount of scatter is introduced. YF_{res} also shows a positive correlation with α between the values of -5 and +5. When $|\alpha|$ is greater than five there is a large amount of scatter in YF_{res} at a given α. Almost all values that have a $YF_{res} > 1$ also show a positive SFH α, i.e. the top left quadrant of the plot is empty. The correlations between YF_{res} and f_{abs} or α implies the young fraction is not the sole physical mechanism responsible for determining. These two quantities also correlate with SFR_{Res}, but it is a noticeably weaker correlation as more scatter is introduced. The scatter in YF_{res} is well explained by f_{abs} and the slope of the recent star formation history however, these may not be the only physical quantities that can explain the behaviour of YF_{res}.

2.4 Discussion

Studies that have investigated the IR properties of simulated galaxies often use a Monte Carlo approach to radiative transfer modeling [45, 77, 14]. This involves tracing many individual photons from each source. In simulated galaxies, the sources are stars and dust in the ISM acts as the absorber/scatterer. As each photon propagates, the density and physical properties of dust at the given position dictate the probability it is absorbed or scattered. Photons are traced until they are absorbed or exit the galaxy. Dust, when heated, acts as an additional source of photons. Many photons from each

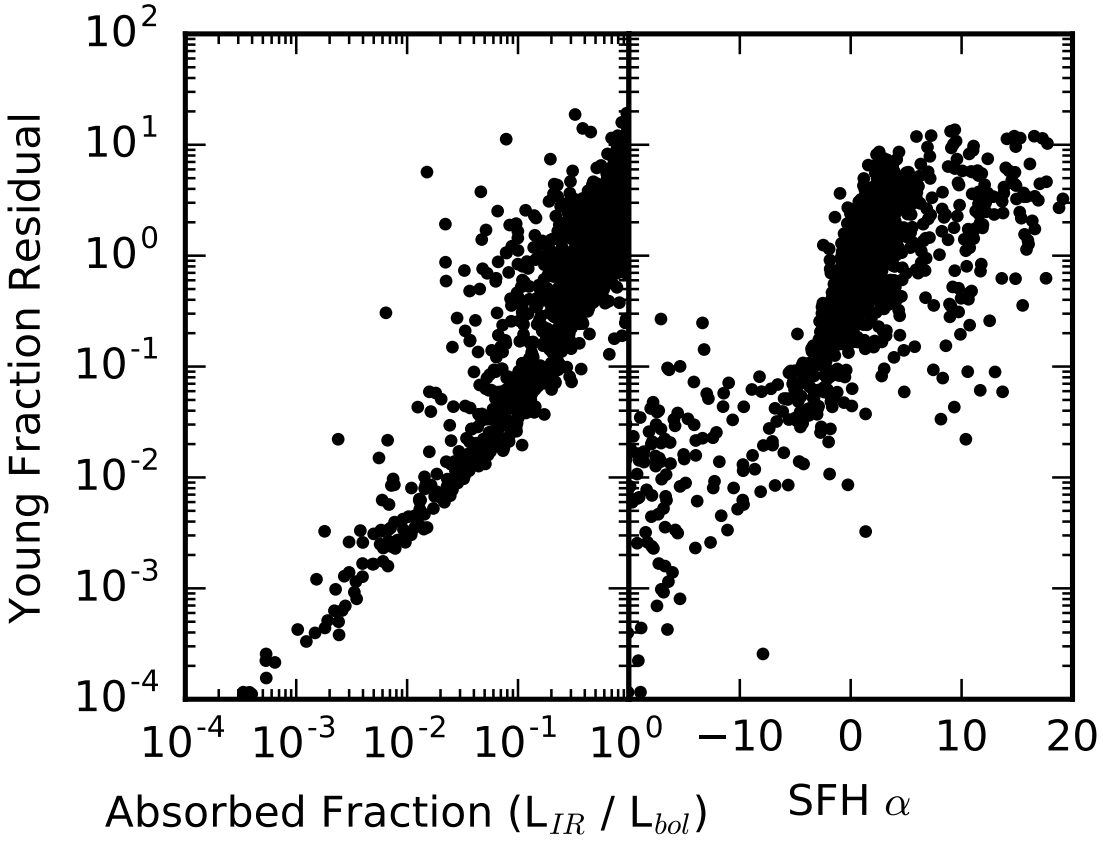

Figure 2.9: The young fraction residual (YF_{res}) is plotted against the absorbed fraction (f_{abs}) and the slope of the recent star formation history (α). $YF_{res}$is the discrepancy between the data and the model shown in Fig. 2.8 and is calculated using Eqn. 2.7. Both variables, f_{abs} and α, correlate well with YF_{res}.

source are traced until the synthetic SED is converged. Arbitrary precision can be achieved with increasing number of photons traced but it is extremely costly. It is also an incredibly flexible method as new physics can be added simply as additional sources or absorbing/scattering probabilities. Examples of publicly available Monte Carlo radiative transfer codes for studying galaxies are *SUNRISE* [56] or *HYPERION* [85], which are used in the studies cited above.

The main advantage of the method used in this study has over traditional Monte Carlo methods is the computational cost. This allows us to estimate L_{IR} for a large sample of galaxies with different characteristics. As mentioned, we can also easily asses the contribution to L_{IR} from different stellar populations. Although this is not

theoretically impossible with Monte Carlo codes, it would be non-trivial to implement. However, since our model is more simplistic many features are lost. Notably, we do not calculate the shape of the IR SED, only the total luminosity. This is sufficient for this study since we are only interested in the L_{IR}-SFR correlation. Synthetic SEDs could be calculated using the framework derived but would require detailed modeling of the dust temperature and emission. Although not universally applicable, the simple model described in § 2.2 offers many advantages for investigating the L_{IR}-SFR correlation.

When binned in SFR and L_{IR}, SFR_{Res} displays slightly different behavior. This is a result of the distribution of $\frac{L_{IR}}{SFR}$ not being centered around the K98 conversion factor. Fig. 2.6 shows the log normal distribution peak at high $\frac{L_{IR}}{SFR}$ values than the K98 model predicts. A galaxy is more likely to scatter up into a L_{IR} bin for a lower SFR than what is expected than it is to scatter down from a higher SFR. For this reason, the mean SFR_{Res} in L_{IR} bins is generally higher than similar SFR bins. This is also affected by the presence of the extremely low SFR_{Res} galaxies at SFR $\sim$ 5 $M_{\odot}yr^{-1}$. When binned in L_{IR}since the lower limit is 10^8 $L_{\odot}$, these galaxies do not contribute. If binned in SFR instead, these galaxies decrease the mean SFR_{Res}. The distribution of $\frac{L_{IR}}{SFR}$ leads to the different behavior if galaxies are binned in SFR or L_{IR}.

Increasing SFR_{Res} with decreasing SFR has also been in observational studies. Totani et al. (2011) [104] use SED fitting to derive accurate star formation rates and compare to L_{IR} for local galaxies in the Sloan Digital Sky Survey. They find broad agreement between SFR_{IR} and SFR_{true} at SFR $>$ 1 $M_{\odot}yr^{-1}$, but find consistent overestimation at lower SFRs. Utomo et al. (2014) [106] preform a similar analysis except for galaxies at $0.5 < z < 2$. They find consistent overestimation at SFR $< 10M_{\odot}yr^{-1}$, growing at lower SFRs which reaches over an order of magnitude at SFR $\sim$ 1 $M_{\odot}yr^{-1}$. Both studies attribute this effect to significant dust heating from old stars. At lower luminosities, a relatively small amount of dust heating by old stars can contribute a large fraction to L_{IR}. However the results from this study, as shown

in Fig. 2.8, suggest that dust heating from old stars may not be the only contributing factor to L_{IR}overestimating SFR.

It is also observed that low SFR galaxies have a larger $\sigma\left(\frac{L_{IR}}{SFR}\right)$. In the FIRE simulations, these galaxies are known to exhibit an incredibly variable SFH [94, 49]. Often a full burst quench cycle happens on a time scale of $\sim$ 100 Myr. This violates one of the assumptions for using L_{IR} as a SFR indicator; that there is a constant star formation history over the past 100 Myr. This is an inherent uncertainty when a time-averaged measure of SFR is used. More massive galaxies, with higher SFRs, in the simulation suite have smoother star-formation histories therefore are less susceptible to this error and show a smaller $\sigma\left(\frac{L_{IR}}{SFR}\right)$.

Interestingly the contribution from old stars is not the sole mechanism driving the behavior of $\sigma\left(\frac{L_{IR}}{SFR}\right)$. Fig. 2.8 displays that while there is a marginal correlation between the IR young fraction and SFR_{Res}, there is a significant amount of scatter. Figure 2.9 shows this scatter is well explained by f_{abs} and the SFH slope. At low YF_{res}, there is a strong positive correlation with f_{abs}. The physical interpretation is that these galaxies have an extremely low dust column density and therefore a large faction of photons from young stars are not absorbed. This breaks one of the assumptions of the K98 model and leads to a severe underestimation of SFR from L_{IR}. At absorbed fraction, the positive YF_{res} can be explained by analyzing the star formation history. All galaxies with a $YF_{res} > 1$ also have a positive SFH α meaning theirs SFRs have been recently rising. This breaks another assumption of the K98 model, that SFR has been constant for the past 100 Myr. An increasing SFH allows the youngest and brightest stars to contribute a significant amount to L_{IR} while the SFR_{100Myr} is depressed by the low SFR at earlier times. The result is a low SFR_{100Myr} while L_{IR} will remain high, leading to $SFR_{Res} > 1$. The absorbed fraction and the SFH are likely correlated so it is difficult to determine which is more important in driving the scatter in SFR/L_{IR}but we have shown that the contribution from old stars is not the only physical mechanism.

Although previous studies have investigated the L_{IR}-SFR correlation in simulations, this is the most complete sample spanning galaxy properties and epochs. Narayanan et al. (2015) [77] attempt to reproduce SMGs by simulating massive halos from $z = 6 - 2$. Although not the main objective of the study, they present a SFR_{true} vs. SFR_{IR} plot. Good agreement is seen at SFRs between 10^2 $M_\odot yr^{-1}$ and 10^3 $M_\odot yr^{-1}$, while at higher SFRs the IR luminosity consistently overestimate the SFR by a factor of two. We also find good agreement between SFR_{IR} and SFR_{true} at $\lesssim 10^3 M_\odot yr^{-1}$ but our galaxy sample is sparse at SFR$> 10^2$ $M_\odot yr^{-1}$ and contains no galaxies at greater than 10^3 $M_\odot yr^{-1}$. Hayward et al. (2014) [45] run idealized simulations of isolated disks and major mergers then post-process with *SUNRISE* to extract synthetic spectra. They find that in isolated disks the IR luminosity accurately traces the SFR but not in mergers, specifically after the galaxies first collide. The overestimation is approximately one order of magnitude and lasts for > 1 Gyr. Both studies attribute the overestimation to significant dust heating by old stars. Camps et al. (2016) [14] preforms dust radiative transfer on $z = 0$ galaxies in the *EAGLE* simulation. They find good agreement between L_{IR} and SFR except for a population of galaxies at SFR< 1 $M_\odot yr^{-1}$. For these galaxies, L_{IR} overestimates SFR and the authors attribute this to emission from diffuse dust in the outskirts of the galaxy. This study generally agrees with previous, more specific, studies of the SFR-L_{IR} correlation in simulated galaxies and expands to a more encompassing sample.

These results urge caution when interpreting observations of galaxies, specifically L_{IR} limited surveys. Selecting IR bright galaxies may not ensure that they have large SFRs as is canonically believed. In the simulated galaxy sample there are 84 luminous infrared galaxies (LIRGs, $10^{11} L_\odot < L_{IR} < 10^{12} L_\odot$). Based on K98, LIRGs should have SFRs of 15 $M_\odot yr^{-1}$ to 150 $M_\odot yr^{-1}$ however, about one third (27 of 84) of our sample of LIRGs have SFR < 10 $M_\odot yr^{-1}$. This is caused by the large spread of SFR at a given L_{IR}, shown in Fig. 2.7. In our simulation sample, and what is observed, the number of galaxies decreases monotonically as L_{IR} increases [69]. Thus, it is more

likely for galaxies with low SFR to scatter to a higher L_{IR} than it is for high SFR galaxies to scatter down, due to the shape of the L_{IR}/SFR distribution and because there are more galaxies at low SFR. This bias should be considered when analyzing results of L_{IR}selected galaxy surveys.

The main issue with a simple conversion for L_{IR} to SFR is that there are many factors that control L_{IR}. Previous studies have shown that both the SFR, the dust mass (M_{dust}) and the dust temperature set the IR luminosity and SED shape of a galaxy. These quantities are all correlated at some level, however these relationships are not necessarily one-to-one and there may be a significant amount of scatter [62]. Recent studies have suggested that SFR alone is not sufficient to estimate L_{IR} and that a secondary term, such as M_{dust}, is required to accurately fit the IR SED. [87, 44]. The FIRE simulations also do not include the physics of AGN feedback, which has been shown to be a significant source of dust heating in some galaxies and could further skew the K98 conversion [76]. Due to the complex nature of galaxies, a simple integrated luminosity does not contain enough information to accurately estimate the SFR in all cases.

Broad band SED fitting offers a more sophisticated method to estimate the SFR. These include publicly available codes such as *CIGALE* [78] or *MAGPHYS* [29], for example. These codes draw from a template SEDs, stellar population and dust attenuation models to fit the entire SED of a galaxy. Ideally this will contain data points ranging from the UV to the IR. Observations in the UV-visible regions help constrain star formation histories, stellar mass and dust attenuation. IR observations help estimate M_{dust} and the amount of obscured star formation. SED fitting codes have shown promise to accurately predict properties of galaxies however there are many implicit assumptions and the results are likely sensitive to the assumed dust and stellar population models [91]. Another alternative to estimate SFR is to measure certain emission line luminosities. For example [CII] which measures cool dense gas that stars form out of [33]. The physical process which drive emission lines is not completely understood and they are difficult to calibrate. Unfortunately, with all

methods to estimate SFR, there are biases and shortcomings that must be understood and considered. Where possible, it is best to estimate SFR through multiple means to compare and contrast the results.

2.5 Conclusion

In this study, we have developed a simple, light and flexible method to estimate L_{IR} from hydrodynamic simulations of galaxies. This method calculates L_{IR} by estimating the luminosity originating from each star particle that will be absorbed by dust. Thus, we can distinguish between the contributions of different stellar populations to the IR luminosity. The algorithm is then applied to the FIRE simulation suite with the goal to investigate commonly used K98 L_{IR} to SFR conversion. The main conclusions of the study are as follows:

- We find that the SFR inferred from L_{IR} by the K98 model (SFR_{IR}) generally overestimates the true SFR. The overestimation is higher in lower SFR galaxies. At < 1 $M_{\odot}yr^{-1}$, there is on average a factor of ~ 2 overestimation, while at SFR $> 10 M_{\odot}yr^{-1}$, SFR_{IR}broadly agrees with the true SFR. This trend has also been seen in observational studies.

- There is significant scatter in L_{IR}/SFR, with $\sigma\left(\frac{L_{IR}}{SFR}\right)$ reaching as high as one order of magnitude at $L_{IR} < 10^9$ $L_{\odot}$. $\sigma\left(\frac{L_{IR}}{SFR}\right)$ decreases with increasing SFR or L_{IR}, reaching ~ 0.2 dex at $L_{IR} > 10^{12}$ $L_{\odot}$. This is likely caused by low SFR galaxies exhibiting a more variable SFH than massive galaxies.

- The distribution of SFR_{Res} ($\frac{SFR_{IR}}{SFR_{true}}$) is not well explained solely by contribution from old stars. This is shown as a large scatter in SFR_{Res} at a given L_{IR} young fraction. We find that this scatter is well explained by differences in absorbed fraction and the slope of recent star formation history. Contribution from old stars is not the sole factor in determining SFR_{Res}.

The idea that L_{IR} is an imperfect tracer of SFR is not new, Kennicutt himself acknowledged several possible problems in his original work, suggesting it may not be

suitable for all galaxies. Yet, since a simple L_{IR} to SFR conversion is widely used it is crucial to understand it's flaws and biases. In general, the results of this study urge caution when interpreting IR observations of galaxies. Especially surveys which select galaxies based on a limiting L_{IR}. The shape of L_{IR}/SFR distribution may cause a non-uniform sample of galaxies being analyzed. When interpreting SFRs of galaxies, it is important to compare and contrast different methods of estimation, such as SED fitting, L_{IR} or emission lines. Each method has it's on inherit biases and flaws which should be acknowledged.

Chapter 3

SPT 2349-56: A Massive and Active Proto-cluster Core

3.1 Introduction

The south pole telescope (SPT) is a 10m telescope located at the south pole. It observes at millimeter wavelengths and is designed to survey large portions of the sky [113]. SPT completed its first major survey in the fall of 2011 and scanned > 2500 deg^2 at wavelengths of 1.4 mm, 2 mm and 3 mm. The main scientific goal of this survey was to search for galaxy clusters by looking for distortions in the cosmic microwave background caused by the Sunyaev-Zel'dovich effect [9]. This effect measure distortions in the cosmic microwave background caused be hot gas (T $> 10^7$ K) in the center of galaxy clusters. A secondary result of this project was a catalog millimeter point sources.

Viera et al. (2010) [108] presented a catalog of such sources which had dust like SEDs in the three observed SPT bands. Later they discovered these sources were SMGs at high-redshift that were gravitationally lensed by foreground galaxies. This boosts the observed flux of the SMGs by a factor of 5-20 [109]. In a series of studies the lensing of these galaxies was modeled and numerous observations accrued [95, 100]. These SMGs provide an interesting view into galaxies formation in the early universe. Gravitational lensing boosts the observed flux which allows many previously difficult observations to become feasible. The SPT-SMG catalog has provided a unique opportunity to study SMGs in great detail.

While over 90% of SPT-SMGs show evidence of being gravitationally lensed, a small population do not. Follow up observations did not discover a foreground galaxy which could be lensing the SMG, implying these systems are intrinsically very bright. These unlensed sources are incredibly interesting as they could represent some of the

brightest mm/sub-mm systems in the high-redshift universe. In particular the source SPT 2349-56 (or SPT 2349) was shown to be of different nature than the other unlensed sources. High resolution but shallow $S_{870\mu m}$ imaging showed that SPT 2349 consists of at least five individual SMGs, and a redshift search found $z = 4.3$ [95, 100]. These initial results suggest that SPT 2349 could represent a proto-cluster in the early universe.

In this study, we present detailed follow-up observations of SPT 2349-56. The primary data was observed at the Atacama large millimeter array (ALMA) aiming to measure 1.1 mm continuum along with CO(4-3) and [CII] emission lines. Observational details and results are shown in §3.2. In §3.3 we compare SPT 2349-56 to similar sub-mm luminous proto-clusters. The observations and comparisons are then discussed and summarized in §3.5.

3.2 Observations

The main observations used in this work were taken at the Atacama large millimeter array (ALMA)[1]. This is a millimeter/sub-millimeter interferometer located in Chile on the Chajnantor plateau. There are over fifty individual 12m dishes that act as a single telescope and can be arranged to cover up to 16 km. This greatly increases the baseline and therefore the resolution of the images. It is the most sensitive and highest resolution mm/sub-mm instrument that exists. Apart from images at different wavelengths, it can also use a spectral scan mode. This scans a field across a given frequency range, up to 4 GHz. The result is a data cube with 3 dimensions: the 2 on-sky directions and frequency.

The primary 1.1 mm imaging for this work was obtained under an ALMA Cycle 4 program (2016.0.00236.T; PI: S. Chapman) targeting SPT 2349-56. The source was observed on December 14th, 2016 in a 40-2 array configuration with baseline lengths of 15m-459m and total on source integration time of 21.67 minutes. Ceres and J2357-5311 were used as flux and phase calibrators respectively. The [CII] line was observed

[1]http://www.almaobservatory.org/en/home/

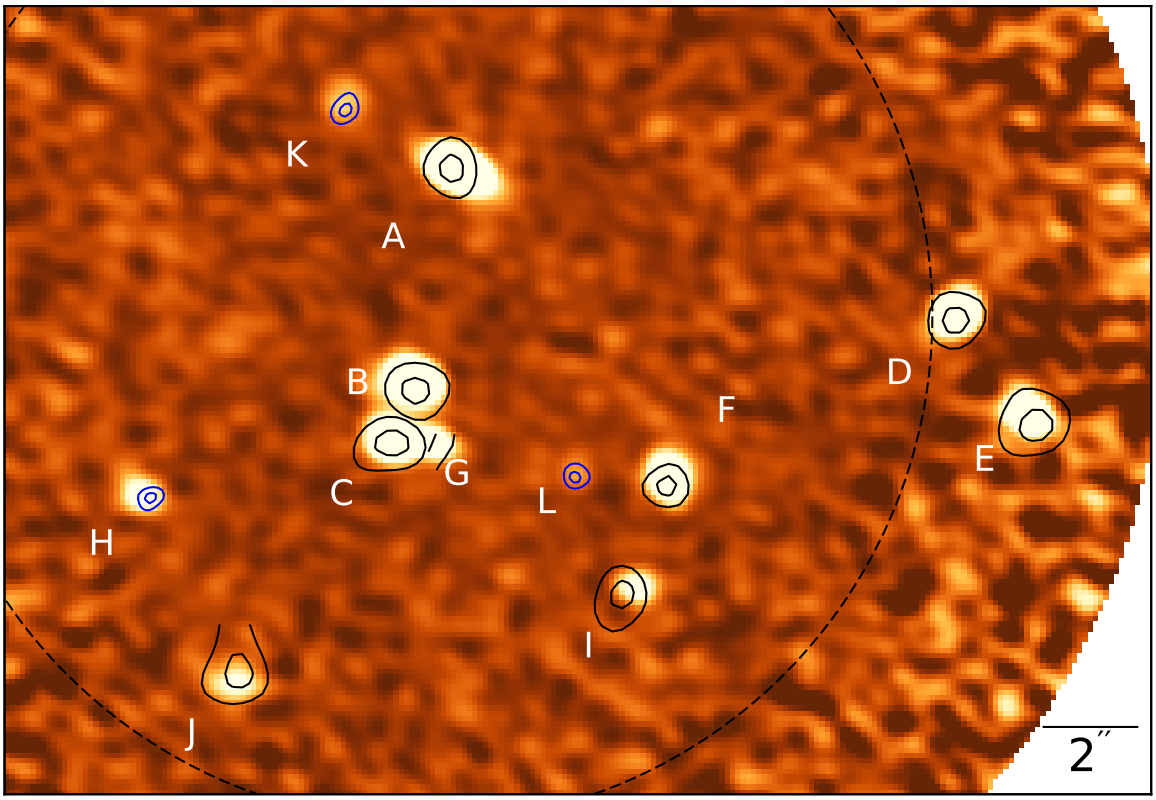

Figure 3.1: ALMA 1.1 mm image displaying the 12 sources detected at $> 5\sigma$ labeled A-L. Black (Blue) contours show the integrated CO(4-3) ([CII]) flux for each source at 60% and 90%. The dotted black line shows where the primary beam is 50% the maximum.

at as part of the same ALMA project on March 23rd, 2017. Again, using Band-7, 356 GHz to 360 GHz was scanned. The setup used a 40-2 array configuration with baselines of 16m-459m. There was a on-source integration time of 13.6 min using J2357-5311 as both the flux and phase calibrator. Observation of CO(4-3) (86 GHz - 88 GHz) was taken using ALMA band 3 under Cycle 3 program 2015.1.01543.T (PI: K. Lacaille). Data was taken on June 24th, 2016 with a 47.37 min integration time. The array used 36 antennas with baselines ranging from 15m to 704m. Pallas and J2343-5626 were used to calibrate the flux and phase respectively. Data was processed using the standard ALMA pipeline using natural beam weighting.

The 1.1 mm image is displayed in Figure 3.1. The black dotted line displays the FWHM of the primary beam. The primary beam can be thought of as the noise in the image as a function of distance from the center of the field. The noise

increases with distance approximately following a Gaussian. 12 individual sources detected using the *Source Extractor* software package [48]. They are labeled A-L with decreasing 1.1mm flux ($S_{1.1mm}$). $S_{1.1mm}$ ranges from 0.23 mJy to 4.63 mJy [2]. All sources are detected with a signal-to-noise ratio (SNR) greater than five. Even though sources D & E lie outside the FWHM of the primary beam they are sufficiently bright to overcome the increasing noise. All of the sources lie with a 12″ radius[3] with a maximum physical separation of 150 kpc. All 12 sources have line detections in CO(4-3) and/or [CII]. Contours show the 60% and 90% levels of the integrated CO(4-3) or [CII] line. High resolution imaging shows that SPT 2349 has revealed it consists of at least 12 individual SMGs.

The CO(4-3) and [CII] spectra for the 12 SMGs are displayed in Figure 3.2. Frequency is converted to velocity using the radio velocity definition, shown below.

$$\mathrm{V} = \mathrm{c}\left(1 - \frac{\nu}{\nu_0}\right) \tag{3.1}$$

Where V is the velocity, c is the speed of light, ν is the frequency and ν_0 is the expected frequency of the line. This is the red shifted frequency of CO(4-3) or [CII] emission i.e. 460 GHz / (1 + 4.3) = 87 GHz and 1.9 THz /(1 + 4.3) = 358 GHz respectively. Spectra are extracted from the center of the line emission for each SMG (This does not necessarily align with the 1.1mm emission but is never offset by more the 1″). Spectra are then smoothed using a Gaussian kernel with FWHM = 100 km s^{-1}.

Figure 3.2 displays that not all of the 12 SMGs are detected in both CO(4-3) and [CII]. Seven SMGs (A,B,C,D,F,I and J) are detected with SNR greater that five in both CO(4-3) and [CII]. In these sources, the two spectra agree well with each other. The SMGs H, K and L are only detected in [CII]. G and E are only detected in CO(4-3) although, E is marginally detected in [CII] at 2.6σ. It lies $\sim$ 13″ from the center of the field increasing the noise by a factor of $\sim$ 3. Extra care was taken when fitting

[2] 1 Jy = 10^{-26} W m^{-2} Hz^{-1}

[3] 1 arc second (″) = 1/60 arc minute (′) = 1/3600 deg

source G as there is significant contamination from galaxy C at V $\sim$ 1000 km s^{-1}. The true spectrum of G is the smaller peak at V $\sim$ 0 km s^{-1}. Gaussian profiles are fit to each line using a least squares method. The velocity dispersions ($\sigma_{\rm V}$) of the SMGs is extracted from the gaussian fit and are found to be typically $\sim$ 200 km s^{-1}, with the largest, galaxy D, reaching $\sim$ 450 km s^{-1}. Through spectroscopy of CO(4-3) or [CII], all 12 SMGs are confirmed to be at $z \sim 4.3$ and members of the same proto-cluster.

The relative velocity (ΔV) of each galaxy is extracted as the peak of the Gaussian profile and is also displayed on each panel in Fig. 3.2. Where detected, ΔV is taken from the CO(4-3) spectra. From the distribution of ΔV, the cluster dispersion is calculated to be 496 ± 141 km s^{-1}. Using the virial theorem and the cluster dispersion we calculate a proto-cluster mass of $2.3 \pm 1.5 \times 10^{13}$ M$_{\odot}$.

The field around SPT 2349 has also been observed in the near-IR. The Infrared Array Camera (IRAC) on board the Spitzer Space Telescope observed at 3.6μm and 4.5μm on August 2nd, 2009. K-band ($\lambda_{\rm eff} = 2.2\mu$m) were obtained from the Giant Magellan Telescope (GMT). These observations was obtained under large programs to follow-up SPT-SMG sources. Greve et al. (2012) [42] obtained observation of SPT2349 using large APEX bolometer array camera (LABOCA). LABOCA images the sky at 870 μm but with lower sensitivity and resolution then ALMA ($\sim$ 20 $''$ compared to $\sim 0.5\,''$).

Near-IR imaging of SPT 2349 is shown in Figure 3.3. The location and relative sizes of the sources A-L are overlaid on each image. None of the 12 sources are detected in the 2.2 μm image. Five sources (A,C,E,J and K) are detected at 3.6 μm, while four (A,C,E and K) are detected at 4.5 μm. Figure 3.4 displays a false color image consisting of these three wavelengths and contours representing the extended 870 μm emission observed by LABOCA. This 870 μm emission separates into two sources: A brighter and larger southern source and a fainter northern source. The high resolution 1.1mm ALMA observations only covers the center of the southern LABOCA source, whose 870μm flux is measured in Greve et al. (2012) [42] to be

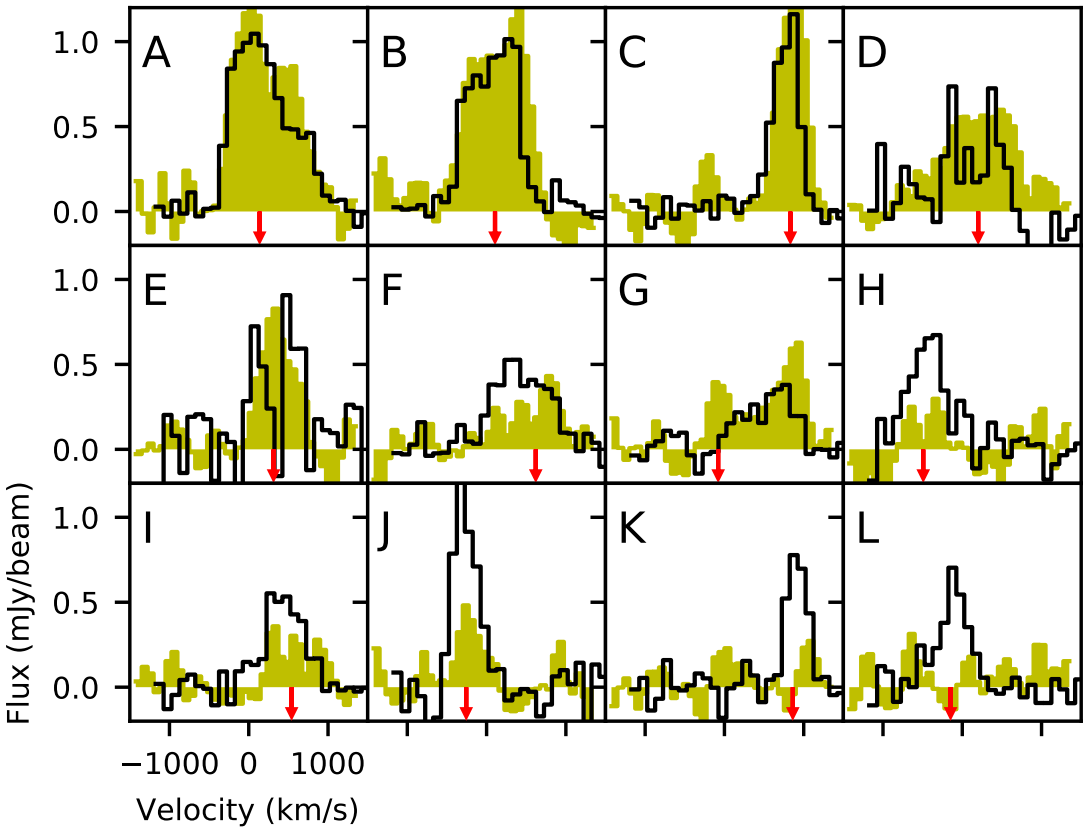

Figure 3.2: Displaying CO(4-3) and [CII] spectrum of for all 12 SMGs, centered at z = 4.3. CO(4-3) spectra are shown in yellow and [CII] spectrum is shown in black. [CII] spectra are depressed by a factor of ten to display alongside the CO(4-3) spectra. The red arrow for each shows the measured velocity offset for each SMG. This is found by fitting a Gaussian to each line profile.

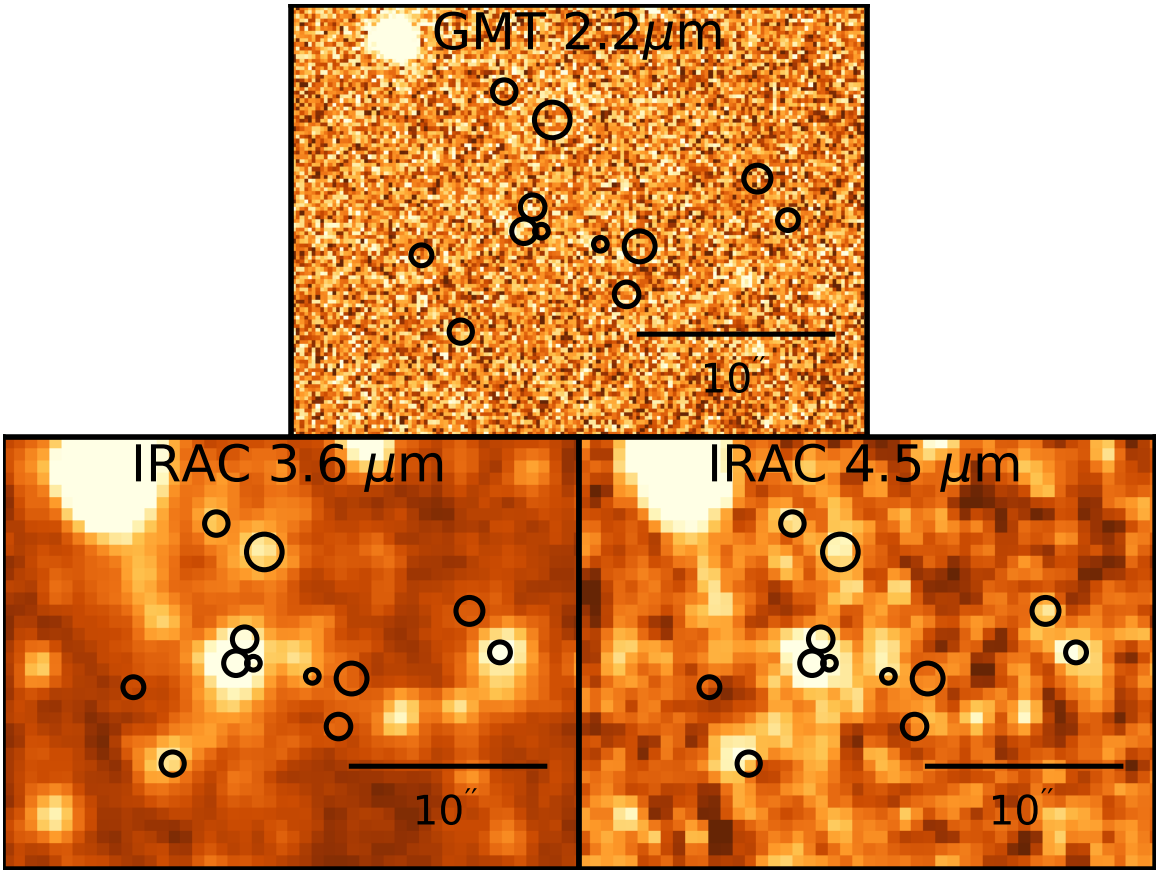

Figure 3.3: Near-IR imaging at 2.2 μm, 3.6 μm and 4.5 μm of SPT 2349-56 is shown. The circles display the location and relative sizes of the proto-cluster SMGs A-L. No sources are detected at 2.2 μm, while five are detected at 3.6 μm and four at 4.5 μm.

56 ± 10 mJy. There is also an elongated northern source present in the LABOCA image whose 870μm flux is measured to be 32 ± 5 mJy. Our current high-resolution ALMA observations only cover a portion of the southern LABOCA source, with the full extent of the 870 μm still to be investigated.

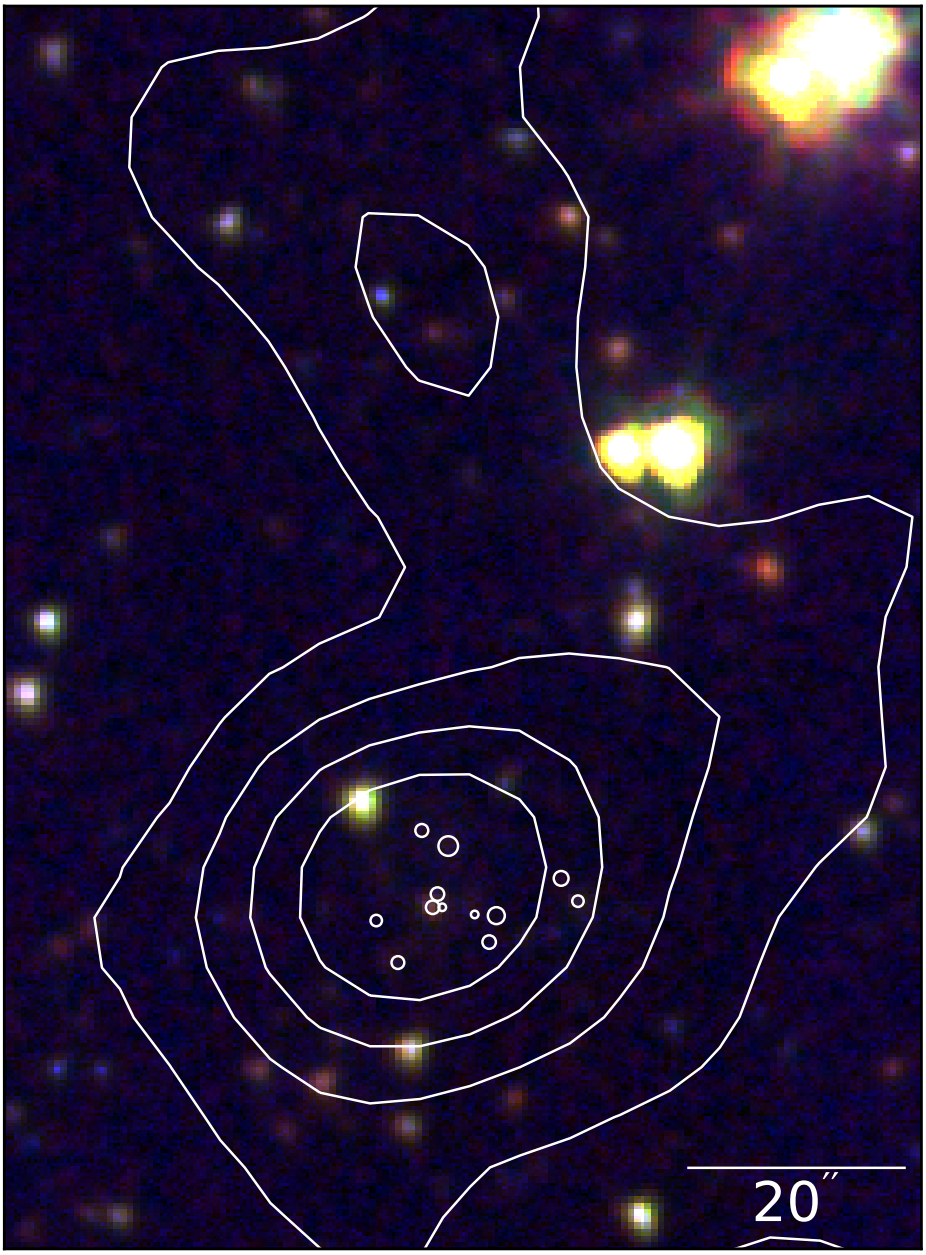

Figure 3.4: LABOCA 870 μm contours overlaid on a 4.5 μm, 3.6 μm, 2.2 μm false color image. Contours represent SNR = 2,5,8 and 11. The white circles show the location and relative sizes of the 12 galaxies A-L detected in the high-resolution ALMA imaging.

Using the set of observations, physical parameters of the galaxies are estimated. To derive SFR we begin by comparing the 1.1 mm flux of the SMGs A,B,C,G and F to their 870 μm flux found in Spilker et al. (2016) [95]. We derive a mean $S_{870\mu m}$ to $S_{1.1mm}$ ratio of 1.5 ± 0.2 which we then use to estimate $S_{1.1mm}$ for the other galaxies. Following Barger et al. (2014) [1] we then convert 870 μm flux to SFR using a scaling of $200\frac{M_\odot yr^{-1}}{mJy}$.

Gas mass is calculated from the CO(4-3) line luminosity, which is converted to CO(1-0) luminosity using $r_{4,1} = 0.41 \pm 0.07$ found in Bothwell et al. (2013) [11]. We use a conversion factor $\alpha_{CO} = 0.8\frac{M_\odot}{K\ kms^{-1}\ pc^2}$ and multiply by 1.36 to account for Helium. Dynamical mass of galaxies is found following Bothwell et al. (2013).

$$M_{dyn}(M_\odot) = 1.56 \times 10^6 \sigma_v^2 R \tag{3.2}$$

Where σ_v is the line of sight velocity dispersion, in km s^{-1} calculated from the Gaussian fit to each line profile and R, the size of the galaxy, is calculated from the FWHM of each line profile where it reaches 50% of the peak flux, in kpc. We use σ_v from the CO(4-3) profile for all sources except H,K and L, where the [CII] profile is used because CO(4-3) is not detected.

Table 3.1: Summarizing all observations of the 12 proto-cluster SMGs identified in the high resolution 1.1mm image.

Source	RA (H:M:S)	DEC (deg:M:S)	1.1 mm flux (mJy)	870 μm flux (mJy)	3.6 μm flux (μ Jy)	4.5 μm flux (μ Jy)	CO(4-3) flux (Jy km/s)	[CII] Luminosity (10^9 $L_\odot$)
A	23:49:42.672	-56:38:19.32	4.63 ± 0.04	8.80 ± 0.25	13.8 ± 0.7	7.5 ± 1.4	0.980 ± 0.030	5.24 ± 0.15
B	23:49:42.792	-56:38:24	4.35 ± 0.04	6.40 ± 0.27	-	-	0.910 ± 0.030	4.47 ± 0.13
C	23:49:42.84	-56:38:25.08	2.69 ± 0.04	4.20 ± 0.37	34.35 ± 0.9	26.4 ± 1.8	0.550 ± 0.020	2.63 ± 0.10
D	23:49:41.424	-56:38:22.56	2.20 ± 0.08	3.50 ± 0.56	-	-	0.680 ± 0.040	2.15 ± 0.46
E	23:49:41.232	-56:38:24.36	2.12 ± 0.11	3.23 ± 0.48	10.6± 0.6	2.6 ± 1.4	0.400 ± 0.020	2.06 ± 0.74
F	23:49:42.144	-56:38:25.8	1.69 ± 0.05	2.00 ± 0.39	-	-	0.300 ± 0.040	2.54 ± 0.21
G	23:49:42.744	-56:38:25.08	1.11 ± 0.04	1.60 ± 0.39	-	-	0.130 ± 0.020	-
H	23:49:43.464	-56:38:26.16	0.85 ± 0.05	1.30 ± 0.20	-	-	-	2.16 ± 0.18
I	23:49:42.216	-56:38:28.32	0.78 ± 0.05	1.19 ± 0.19	-	-	0.180 ± 0.030	1.89 ± 0.19
J	23:49:43.224	-56:38:30.12	0.61 ± 0.06	0.93 ± 0.16	5.0 ± 0.5	-	0.150 ± 0.020	2.25 ± 0.17
K	23:49:42.96	-56:38:17.88	0.34 ± 0.04	0.52 ± 0.10	7.3 ± 0.5	4.6 ± 1.0	-	1.51 ± 0.10
L	23:49:42.384	-56:38:25.8	0.23 ± 0.04	0.35 ± 0.08	-	-	-	1.65 ± 0.12

Table 3.2: Summarizing known physical properties of the 12 proto-cluster SMGs identified in the high resolution 1.1mm image.

Source	ΔV (km s^{-1})	SFR ($M_\odot yr^{-1}$)	M_{gas} (10^9 $M_\odot$)	M_{dyn} (10^{11} $M_\odot$)
A	138 ± 40	1760 ± 443	20.1 ± 3.5	9.18 ± 0.62
B	106 ± 33	1280 ± 325	18.6 ± 3.3	8.72 ± 0.44
C	832 ± 14	840 ± 223	11.2 ± 2.0	1.66 ± 0.07
D	201 ± 54	700 ± 208	13.9 ± 2.5	16.22 ± 1.30
E	313 ± 26	647 ± 188	8.2 ± 1.5	3.20 ± 0.17
F	620 ± 103	400 ± 127	6.1 ± 1.3	9.34 ± 1.71
G	-79 ± 44	320 ± 112	2.6 ± 0.6	0.64 ± 0.21
H	-492 ± 28	259 ± 76	-	1.79 ± 0.23
I	541 ± 90	238 ± 70	3.8 ± 0.9	4.94 ± 0.90
J	-257 ± 40	186 ± 56	3.1 ± 0.7	1.21 ± 0.17
K	862 ± 12	104 ± 33	-	0.62 ± 0.05
L	-147 ± 18	70 ± 24	-	1.09 ± 0.11

Our observations of the 12 proto-cluster galaxies are summarized in Table 3.1 and the known physical properties are shown in Table 3.2. The SFRs of the galaxies range from 70 $M_\odot yr^{-1}$ up to 1760 $M_\odot yr^{-1}$ totaling over 6800 $M_\odot yr^{-1}$. The proto-cluster contains 4 galaxies with M_{gas} over 10^{10} $M_\odot$ and a total gas mass of 8.8×10^{10} $M_\odot$. The dynamical masses range from $\lesssim 10^{11}$ $M_\odot$ for the fainter sources to 1.6×10^{12} $M_\odot$ for source D. However, some of the brighter sources, specifically A, B and D show strong evidence of rotation. This would imply that our estimate of the dynamical mass is inaccurate. Further analysis is required to investigate and quantify this rotation. SPT2349 contains truly incredible the amount of star formation and gas mass contained in a small volume.

3.3 Comparison

To compare SPT2349 to other systems we begin by analyzing SMG rich proto-clusters at $2 < z < 4$. The sample will be briefly introduced here but we direct the reader to the recent compilation from Casey (2016) [20] for more detail. The GOODS-N proto-cluster at $z = 1.99$ was originally found by Blain et al. (2004) [8] and Chapman et al. (2009) [24]. This 10′ by 10′ field in the Hubble Deep Field North contains 6 SMGs in $\Delta z = 0.008$. The probably of finding this large and overdensity

being drawn from the field distribution by chance is $< 10^{-2}$ %. Interestingly only a modest overdensity of less extreme galaxies is found. MRC1138 was originally discovered by Kurk et al. (2000) [66]. Follow up observations preformed by Kuiper et al. (2011) [65] and Dannerbauer et al. (2014) [32] reveled the presence of 5 SMGs along with an AGN known as the 'Spiderweb galaxy'. The SSA22 proto-cluster was one of the first discovered by Steidel et al (1998) [98], it is extremely extended at $z = 3.09$ with galaxies extending to greater the 15 Mpc [43]. Sub-mm observations of the field have revealed a population of at least eight SMGs. [25, 41, 102, 105]. Two distinct proto-clusters have been detected in the COSMOS field at redshifts of 2.1 and 2.47. COSMOS is an incredibly well studied field with over 30 bands of different wavelength observations available. The z=2.1 proto-cluster was identified by Yuan et al. (2014) [114] and sub-mm follow-up was preformed by Casey et al. (2012) [17] and Hung et al. (2016) [54] which revealed nine SMGs spectroscopically confirmed to reside in the proto-cluster. An overdensity of SMGs, reported by Casey et al. (2015) [18], signifies another proto-cluster in the COSMOS field at $z = 2.47$. This structure contains seven SMGs and is one of the most extended proto-clusters, covering almost half a degree on the sky.

Recently, there have also been detections of SMG overdensities at $z > 4$. The first, GN20 at $z = 4.05$, was discovered by Daddi et al (2009) [31] through the serendipitous detection of CO(4-3) from two SMGs. Although there are 5 SMGs present at this redshift, we focus on the group of 3 SMGs in a group GN20, GN20.2A and GN20.2B as they are physically separated from the other two. HDF850 contains only a single SMG along with 11 spectroscopically confirmed members. Redshift confirmation of $z = 5.18$ was first presented in Walter et al. (2012) [111]. Similarly the AzTEC-3 overdensity is centered on a single SMG at $z = 5.3$ with 12 spectroscopically confirmed members [15]. This is a particularly dense structure with all 13 galaxies residing within a $0.5'$ radius.

To compare SPT 2349 to the sample described above, we plot the $S_{870\mu m}$ number counts in Figure 3.5. This represents the number density of SMGs above a given

$S_{870\mu m}$ in each proto-cluster. The sample described above, SPT 2349 and random field counts from Simpson et al. (2015) [90] are plotted. Error bars are assigned based on poison noise. SPT 2349 stands out far above the rest of the sample and the field measurements. Across the entire flux range, SPT 2349 is approximately 50 times denser than the field measurement and other proto-clusters. While most of the literature proto-clusters have an approximately 10^2 deg^{-2} galaxy density a few stand out above the rest, namely Aztec3 and GN20. These two proto-clusters have the most comparable density to SPT 2349 at higher fluxes but have no detected galaxies with $S_{870\mu m} \lesssim 8$ mJy. They are similar to SPT 2349 in that they are constrained to a small on sky area, however only contain a few luminous SMGs. SPT 2349 is shown to be the densest collection of SMGs ever observed clearly standing out above other SMG-rich proto-clusters.

Figure 3.6 displays the total $S_{870\mu m}$ for each proto-cluster vs the on-sky area. Curve of growth lines show how the flux is built up from individual sources. This is calculated starting from the mean position of SMGs in each proto-cluster and moving radially outwards. For SPT 2349 we show the 12 SMGs from Fig. 3.1 along with the sum of the two extended LABOCA sources shown in Fig. 3.4. Although some of the other proto-clusters have the same or larger total $S_{870\mu m}$ as SPT 2349, they are significantly more extended. The maximum separation between SMGs in SPT 2349 is ~ 150 kpc. In larger proto-clusters, SSA22 for example, the maximum separation is on the order of one Megaparsec. This is what drives the discrepancy in the number density shown in Fig. 3.5. Not that SPT2349 has more SMGs, but simply because they exist in a much smaller area. It's on sky area is $\sim 2 \times 10^4$ kpc^2 compared to the most extended proto-clusters which reach $\sim 10^8$ kpc^2. When the two LABOCA sources are accounted for SPT 2349 rivals some of the most luminous 870 μm systems. The northern LABOCA source is not yet confirmed at $z = 4.3$, so more observations are necessary to investigate.

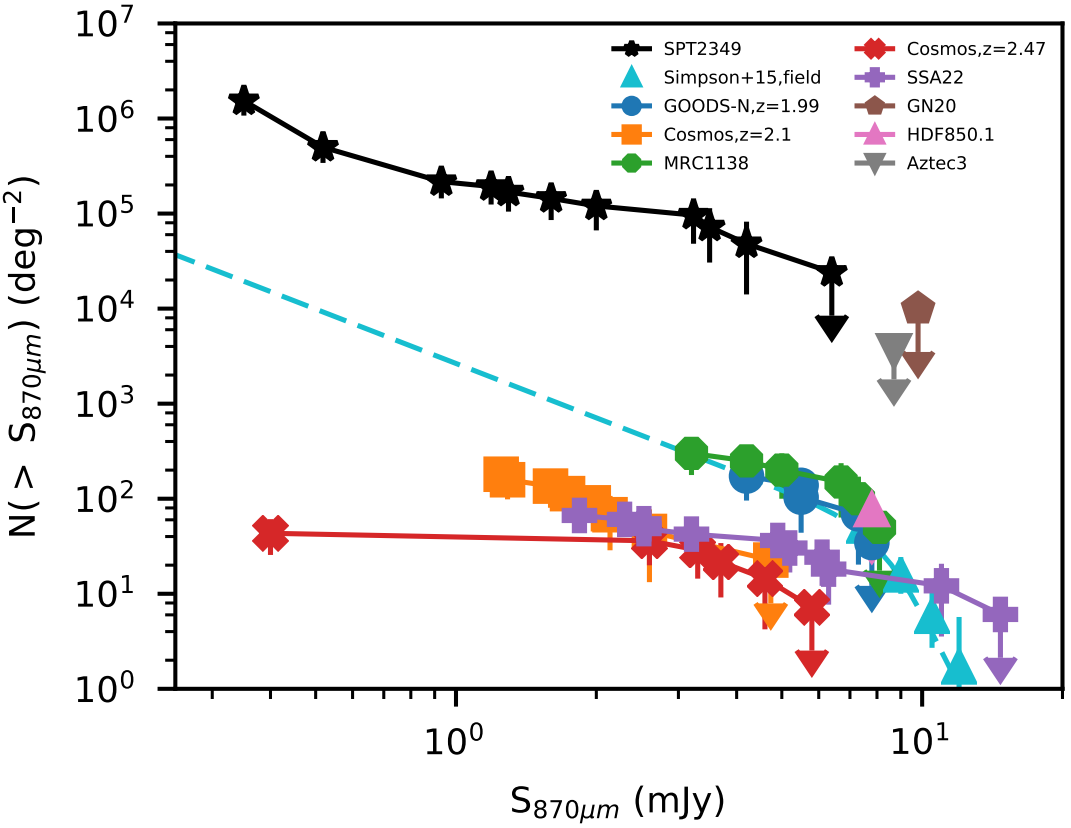

Figure 3.5: Displaying the cumulative 870 μm number density for SPT2349 and other SMG-rich proto-clusters at high redshift. SPT 2349 stands out above the rest as the densest proto-cluster across the entire flux range.

Also shown on Fig. 3.6 is a theoretical prediction for the most luminous protocluster regions. This is generated by analyzing MultiDark, a dark matter only simulation originally ran by Prada et al. (2012) [83]. We choose this simulation as it is one of the largest (2.91 Gpc^3) while still resolving SMG-like halos ($M_{halo} \approx 10^{12}$ $M_\odot$). However, this is only slightly larger than the volume probed by the SPT survey. A specific snapshot at z = 4.68, the closet publicly available snapshot to z=4.3, is analyzed. Halo catalogs were created using the Rockstar halo finder, described in Behroozi et al. (2011) [4]. SFR and M_* are assigned to dark matter halos using the abundance matching formalism described in Behroozi et al. (2013) [3]. The properties are assigned with scatter drawn from a Gaussian distribution with a mean of 2 and standard deviation of 1. This random number is then multiplied by the error given in Behroozi et al. (2013). This distribution is chosen to simulate the starburst properties of the galaxies observed in SPT 2349. $S_{870\mu m}$ is calculated from M_* and SFR following Hayward et al. (2013) [46]. The formula used is shown below.

$$S_{870\mu m} = 0.81 \text{ mJy } \left(\frac{SFR}{100 \text{ } M_\odot yr^{-1}}\right)^{0.43} \left(\frac{M_{dust}}{10^8 \text{ } M_\odot}\right)^{0.54} \tag{3.3}$$

Where $S_{870\mu m}$ is the observed 870 μ m flux, SFR is the star formation rate and $M_{dust}$is the dust mass. This equation was derived by using idealized hydrodynamic simulations of isolated galaxies and galaxy mergers. Dust Radiative transfer was then preformed using *SUNRISE* and this fitting function was derived. The SFR of each halo is known from the abundance matching calculation and M_{dust} is estimated from stellar mass using observed gas fraction and metallicity relations. Once $S_{870\mu m}$ has been assigned to each halo, we search the entire snapshot for the most luminous regions. We begin at each independent halo and calculate to total $S_{870\mu m}$ of all halos within a given radius r. We record the largest total $S_{870\mu m}$ in the entire snapshot for each radius. The mean and 1σ standard deviation of 15 Monte-Carlo iterations is shown in Fig 3.6.

This prediction severely under predicts the amount of flux present in SPT2349. Considering only the area probed by the high-resolution ALMA observations, this

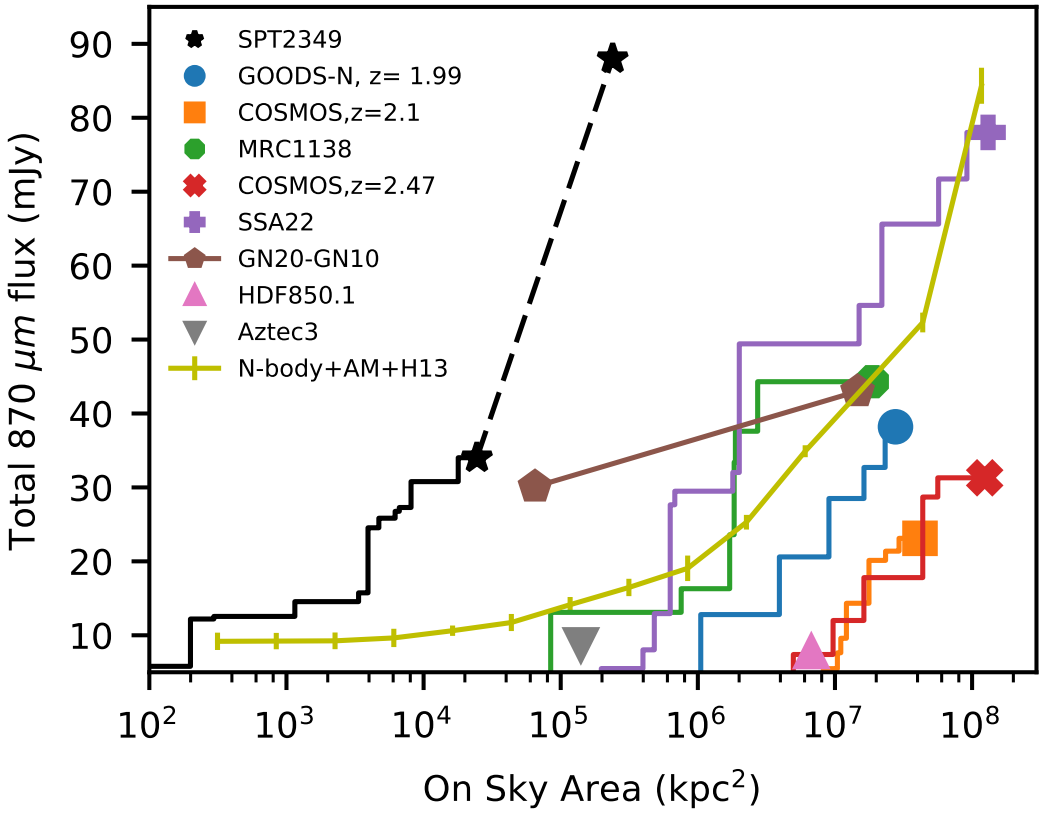

Figure 3.6: The total $S_{870\mu m}$of each proto-cluster vs the physical on-sky area is shown for SPT 2349 and other SMG rich proto-clusters at high redshift. Although SPT 2349 is not the brightest, it is confined to the smallest area. However, it rivals the brightest proto-clusters when the total flux of the two LABOCA sources is considered. A theoretical prediction for the brightest regions at $z \approx 4.5$ is shown to severely underestimate the flux of SPT 2349.

simple model under predicts the amount of observed flux in SPT2349 by 20 mJy. The situation is worse when the LABOCA sources are considered as there is a $\sim$ 60 mJy discrepancy between the prediction and what is observed. Even when the abundance matching relations are applied an average of 2 σ above the mean, this model cannot reproduce the density of SMGs present in SPT2349. The difference arises not from the individual luminosity of each SMG, but the density of galaxies. In the simulation, there is no system with greater than 10 galaxies within a 10^5 kpc^2 area. The existence of this dense collection of SMGs puts stringent constraints on models hoping to explain the evolution of galaxy clusters.

The mass of the proto-cluster sample is plotted against redshift in Figure 3.7. Also shown is a collection of massive galaxy clusters at $z < 2$ [12, 86, 10]. The shaded region is produced in Chiang et al. (2013) [26], who study proto-clusters by directly tracking the evolution of halos with $M_{halo} > 10^{15} M_{\odot}$ at $z = 0$ in N-body simulations. The $\pm 1\sigma$ of the average most massive progenitor at a given redshift is shown. All proto-clusters at $2 < z < 3$ lie on or above the Chiang et al. prediction. At $z > 4$ the literature proto-clusters are below the Chiang et al. prediction except for SPT 2349 which is approximately half an order of magnitude above the mean at $z = 4.3$. It appears that SPT 2349 along with other SMG rich proto-clusters reside on the same evolutionary track with some of the most massive galaxy clusters at $z < 2$. The slope of the Chaing et al. prediction seems to connect them all.

3.4 Discussion

Even though we have detected 12 individual sources using high-resolution ALMA observations, we still do not recover the entire LABOCA flux. Sources A-L total $S_{870\mu m} = 34 mJy$, While the southern LABOCA source has a measured $S_{870\mu m}$ of 56 $\pm$ 10 mJy. Approximately 20 mJy of flux is unaccounted for, implying there may be even more galaxies we have yet to discover. From Fig. 3.4 it appears these galaxies would likely be to the northeast of the already detected SMGs as the LABOCA source is elongated along this direction. There is also the northern LABOCA source which increases the flux that is unaccounted for up to > 50 mJy. However, this northern source does not have a redshift identification and requires further observations to asses whether it resides in the proto-cluster. SPT 2349 already contains an incredible collection of SMGs and we may only be observing the tip of the iceberg.

Theoretical studies of N-body simulations have shown that the progenitors of $M_{halo} > 10^{15}$ $M_{\odot}$ clusters present at $z = 0$ should extend to radii of $\gtrsim 3$ Mpc at $z > 2$[26, 79]. Since SPT 2349 is concentrated to a small volume, it is difficult to asses its exact evolution. Specifically, Chiang et al. warn of interpreting a small overdense region at high-redshift as a "proto-cluster core". Their study reveals that

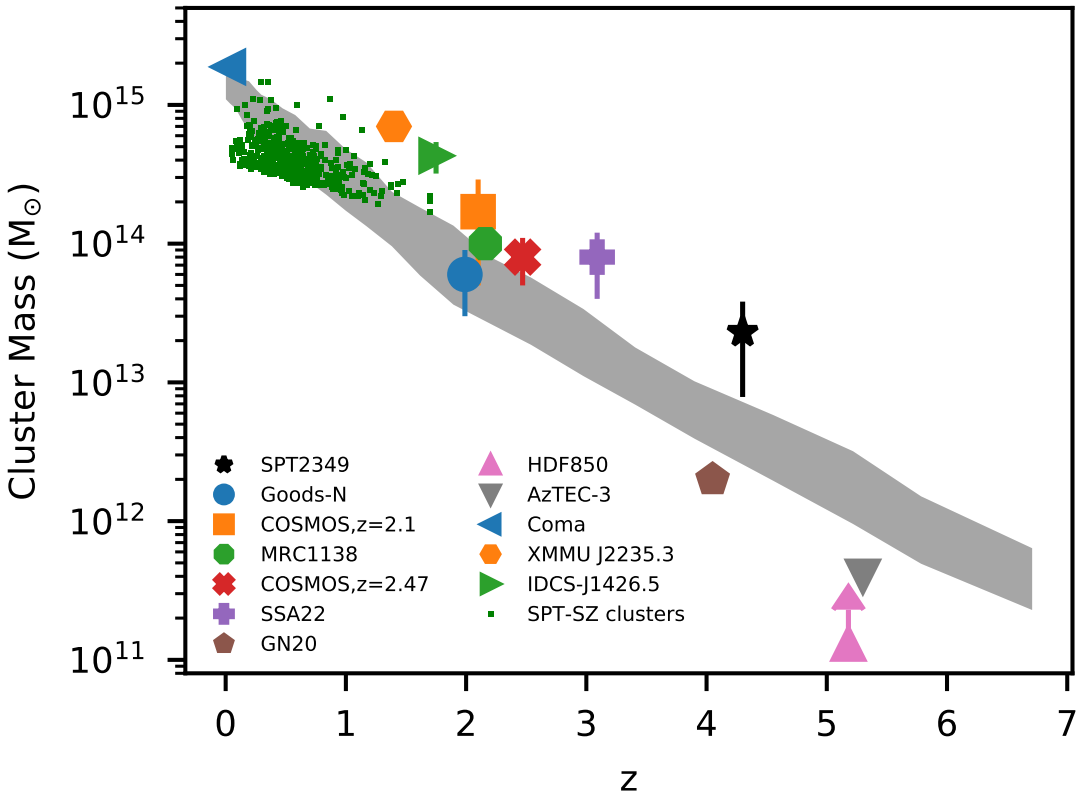

Figure 3.7: The halo mass of SMG rich proto-clusters at high redshift along with the most massive galaxy clusters at $z < 2$ is shown [12, 86, 10]. We also show the mean prediction of most massive progenitor mass vs. z relation taken from the Chiang et al. 2013 study of proto-clusters in N-body simulations. SPT2349 and several other proto-cluster lie at a similar or higher mass than what is predicted.

a small overdense region at high redshift can evolve into a range of masses at $z = 0$. They suggest investigating if the overdensity extends to larger scale (> 3 Mpc) to better predict if it will form into a galaxy cluster. At high redshift, this is difficult as the excess of galaxies will be less pronounced on larger scales and it is challenging to consistently detect low-luminosity galaxies. It is difficult to asses the evolution of SPT 2349 without further observations.

Given the slope of the Chiang et al. prediction in Fig. 3.7 it appears that SPT2349 will evolve into a $\sim 5 \times 10^{15}$ $M_\odot$ halo at $z = 0$. However, we caution the reader against this simple interpretation. Studies have shown that it is nearly impossible to reliably predict the specific evolution of a individual halo. Due to mergers and a complex formation history, halos of a similar mass may follow vastly different evolutions. Therefore predicting the $z = 0$ halo mass based on the mass at a earlier epoch is extremely inconsistent [2, 27]. This uncertainty is exaggerated at high redshift as there is longer for halos to evolve along different paths. Given our observation only span 20 $''$ it is even more difficult to asses it's evolution. Further observations of the surrounding field will reveal if SPT 2349 lies in a larger overdensity on scales $\gtrsim 1$ Mpc, implying it truly is a progenitor of a massive galaxy cluster. If this is not observed, it may be that SPT 2349 represents a smaller group of galaxies caught in a short-lived and extremely active evolutionary phase. The high mass and density of galaxies seen in SPT2349 is suggestive that it is the progenitor of a massive galaxy cluster but it is impossible know for certain.

3.5 Conclusion

The 2500 deg^2 SPT survey discovered many millimeter point sources with dust like SEDs. The majority ($> 90\%$) of these sources were found to be SMGs that were gravitationally lensed by a factor of 5-20 by foreground galaxies. However, some were found to have no evidence of lensing and instead are intrinsically very bright. One of these unlensed SMGs is SPT 2349-56. This study presents high resolution ALMA 1.1 mm imaging and spectroscopy of CO(4-3) and [CII] of SPT 2349-56. The main

results can be summarized as follows:

- We find SPT 2349-56 breaks up into 12 individual SMGs suggesting it likely represent a proto-cluster in the early universe. These SMGs have $S_{1.1mm}$ ranging from 0.23 mJy up to 4.63 mJy. All 12 galaxies have CO(4-3) and/or [CII] detections and are confirmed to be part of the same proto-cluster structure at $z = 4.3$.

- These SMGs are gas rich with a total $M_{gas} = 8.8 \times 10^{10}$ $M_{\odot}$ and are incredibly active with a total SFR = 6800 $M_{\odot}yr^{-1}$. A cluster dispersion of 496±141 km s^{-1} is measured implying a proto-cluster mass of $(2.3 \pm 1.5) \times 10^{13}$ $M_{\odot}$.

- By comparing to other SMG rich proto-clusters, we find that SPT2349 represents the densest collection of SMGs observed. Other proto-clusters may contain a similar number of SMGs but are extended on considerably larger scales ($\gtrsim 1$ Mpc or 0.5 deg). Whereas in SPT2349 exists in a much more confined area with a maximum on sky separation of ~ 150 kpc.

SPT 2349-56 contains a truly extraordinary collection of SMGs. This source presents a unique laboratory to study galaxy formation in the early universe as it may represent an incredibly active phase in the evolution of a massive galaxy cluster. The existence of this system places stringent constraints on galaxy formation models. Further observations will help investigate the full extent proto-cluster and surrounding field giving insight into its evolution. SPT 2349-56 represents a fascinating source at high redshift and will help decode the mystery of how proto-clusters form and grow.

Chapter 4

Conclusion

In this thesis, I present two projects concerning IR emission of galaxies: Star formation rate indicators in the FIRE simulations and SPT 2349-56: a massive and active proto-cluster core. In the first project, L_{IR} is calculated by post-processing the FIRE simulations. This is then used to test the commonly used linear conversion between L_{IR} and SFR. In bright and actively star forming galaxies this conversion is shown to perform well however, at low SFR, L_{IR} consistently overestimates the true SFR. A significant amount of scatter in L_{IR}/SFR across the whole sample is observed. This behavior is driven by dust heating by old stars, differences in absorbed fraction and the star formation history. The latter project involves characterizing the source SPT 2349-56. High resolution ALMA imaging reveals that it contains at least 12 SMGs and likely represents a proto-cluster in the early universe. This is one of the densest collection of SMGs ever observed as all 12 galaxies are confined to a $\sim 12''$ radius. Further observations of the surrounding field will determine if this overdensity extends on larger scales and help interpret SPT 2349-56's evolution.

Bibliography

[1] A. J. Barger, L. L. Cowie, C. C. Chen, F. N. Owen, W. H. Wang, C. M. Casey, N. Lee, D. B. Sanders, and J. P. Williams. Is There a Maximum Star Formation Rate in High-Redshift Galaxies? *The Astrophysical Journal*, 784(1), jan 2014.

[2] Peter Behroozi, Danilo Marchesini, Risa Wechsler, Adam Muzzin, Casey Papovich, and Mauro Stefanon. Using Cumulative Number Densities to Compare Galaxies across Cosmic Time. *The Astrophysical Journal Letters, article id. L10, 5 pp. (2013).*, 777(1), aug 2013.

[3] Peter S. Behroozi, Risa H. Wechsler, and Charlie Conroy. THE AVERAGE STAR FORMATION HISTORIES OF GALAXIES IN DARK MATTER HALOS FROM z = 0-8. *The Astrophysical Journal*, 770(1):57, jun 2013.

[4] Peter S. Behroozi, Risa H. Wechsler, and Hao-Yi Wu. The Rockstar Phase-Space Temporal Halo Finder and the Velocity Offsets of Cluster Cores. *The Astrophysical Journal*, 762(2), oct 2011.

[5] G. J. Bendo, M. Baes, S. Bianchi, M. Boquien, A. Boselli, A. Cooray, L. Cortese, I. De Looze, S. di Serego Alighieri, J. Fritz, G. Gentile, T. M. Hughes, N. Lu, C. Pappalardo, M. W.L. Smith, L. Spinoglio, S. Viaene, and C. Vlahakis. The identification of dust heating mechanisms in nearby galaxies using Herschel 160/250 and 250/350μm surface brightness ratios. *Monthly Notices of the Royal Astronomical Society*, 448(1):135–167, sep 2015.

[6] P. N. Best, C. R. Kaiser, T. M. Heckman, and G. Kauffmann. AGN-controlled cooling in elliptical galaxies, may 2006.

[7] Andrew W. Blain, V. E. Barnard, and Scott C. Chapman. Submillimetre and far-infrared spectral energy distributions of galaxies: The luminosity-temperature relation and consequences for photometric redshifts. *Monthly Notices of the Royal Astronomical Society*, 338(3):733–744, sep 2003.

[8] Andrew W. Blain, Scott C. Chapman, Ian Smail, and Rob Ivison. Clustering of Submillimeterselected Galaxies. *The Astrophysical Journal*, 611(2):725–731, may 2004.

[9] L. E. Bleem, B. Stalder, T. de Haan, K. A. Aird, S. W. Allen, D. E. Applegate, M. L. N. Ashby, M. Bautz, M. Bayliss, B. A. Benson, S. Bocquet, M. Brodwin, J. E. Carlstrom, C. L. Chang, I. Chiu, H. M. Cho, A. Clocchiatti, T. M. Crawford, A. T. Crites, S. Desai, J. P. Dietrich, M. A. Dobbs, R. J. Foley, W. R. Forman, E. M. George, M. D. Gladders, A. H. Gonzalez, N. W. Halverson, C. Hennig, H. Hoekstra, G. P. Holder, W. L. Holzapfel, J. D. Hrubes, C. Jones,

R. Keisler, L. Knox, A. T. Lee, E. M. Leitch, J. Liu, M. Lueker, D. Luong-Van, A. Mantz, D. P. Marrone, M. McDonald, J. J. McMahon, S. S. Meyer, L. Mocanu, J. J. Mohr, S. S. Murray, S. Padin, C. Pryke, C. L. Reichardt, A. Rest, J. Ruel, J. E. Ruhl, B. R. Saliwanchik, A. Saro, J. T. Sayre, K. K. Schaffer, T. Schrabback, E. Shirokoff, J. Song, H. G. Spieler, S. A. Stanford, Z. Staniszewski, A. A. Stark, K. T. Story, C. W. Stubbs, K. Vanderlinde, J. D. Vieira, A. Vikhlinin, R. Williamson, O. Zahn, and A. Zenteno. Galaxy Clusters Discovered via the Sunyaev-Zel'dovich Effect in the 2500-square-degree SPT-SZ survey. *The Astrophysical Journal Supplement*, 216(2), sep 2014.

[10] S. Bocquet, A. Saro, J. J. Mohr, K. A. Aird, M. L. N. Ashby, M. Bautz, M. Bayliss, G. Bazin, B. A. Benson, L. E. Bleem, M. Brodwin, J. E. Carlstrom, C. L. Chang, I. Chiu, H. M. Cho, A. Clocchiatti, T. M. Crawford, A. T. Crites, S. Desai, T. de Haan, J. P. Dietrich, M. A. Dobbs, R. J. Foley, W. R. Forman, D. Gangkofner, E. M. George, M. D. Gladders, A. H. Gonzalez, N. W. Halverson, C. Hennig, J. Hlavacek-Larrondo, G. P. Holder, W. L. Holzapfel, J. D. Hrubes, C. Jones, R. Keisler, L. Knox, A. T. Lee, E. M. Leitch, J. Liu, M. Lueker, D. Luong-Van, D. P. Marrone, M. McDonald, J. J. McMahon, S. S. Meyer, L. Mocanu, S. S. Murray, S. Padin, C. Pryke, C. L. Reichardt, A. Rest, J. Ruel, J. E. Ruhl, B. R. Saliwanchik, J. T. Sayre, K. K. Schaffer, E. Shirokoff, H. G. Spieler, B. Stalder, S. A. Stanford, Z. Staniszewski, A. A. Stark, K. Story, C. W. Stubbs, K. Vanderlinde, J. D. Vieira, A. Vikhlinin, R. Williamson, O. Zahn, and A. Zenteno. Mass Calibration and Cosmological Analysis of the SPT-SZ Galaxy Cluster Sample Using Velocity Dispersion and X-ray Measurements. *The Astrophysical Journal*, 799(2), jul 2014.

[11] M. S. Bothwell, Ian Smail, S. C. Chapman, R. Genzel, R. J. Ivison, L. J. Tacconi, S. Alaghband-Zadeh, F. Bertoldi, A. W. Blain, C. M. Casey, P. Cox, T. R. Greve, D. Lutz, R. Neri, A. Omont, and A. M. Swinbank. A survey of molecular gas in luminous sub-millimetre galaxies. *Monthly Notices of the Royal Astronomical Society*, 429(4):3047–3067, may 2013.

[12] M. Brodwin, A. H. Gonzalez, S. A. Stanford, T. Plagge, D. P. Marrone, J. E. Carlstrom, A. Dey, P. R. Eisenhardt, C. Fedeli, D. Gettings, B. T. Jannuzi, M. Joy, E. M. Leitch, C. Mancone, G. F. Snyder, D. Stern, and G. Zeimann. IDCS J1426.5+3508: Sunyaev-Zel'dovich Measurement of a Massive IR-selected Cluster at z=1.75. *The Astrophysical Journal*, 753(2), may 2012.

[13] J. A. Calanog, J. Wardlow, Hai Fu, A. Cooray, R. J. Assef, J. Bock, C. M. Casey, A. Conley, D. Farrah, E. Ibar, J. Kartaltepe, G. Magdis, L. Marchetti, S. J. Oliver, I. Perez-Fournon, D. Riechers, D. Rigopoulou, I. G. Roseboom, B. Schulz, Douglas Scott, M. Symeonidis, M. Vaccari, M. Viero, and M. Zemcov. Far-IR Emission From Dust-Obscured Galaxies. *The Astrophysical Journal*, 7751, apr 2013.

[14] Peter Camps, James W. Trayford, Maarten Baes, Tom Theuns, Matthieu Schaller, and Joop Schaye. Far-infrared and dust properties of present-day galaxies in the EAGLE simulations. *Monthly Notices of the Royal Astronomical Society*, 462(1):1057–1075, jul 2016.

[15] Peter L. Capak, Dominik Riechers, Nick Z. Scoville, Chris Carilli, Pierre Cox, Roberto Neri, Brant Robertson, Mara Salvato, Eva Schinnerer, Lin Yan, Grant W. Wilson, Min Yun, Francesca Civano, Martin Elvis, Alexander Karim, Bahram Mobasher, and Johannes G. Staguhn. A massive protocluster of galaxies at a redshift of z 5.3. *Nature*, 470(7333):233–235, jan 2011.

[16] Chris Carilli and Fabian Walter. Cool Gas in High Redshift Galaxies. *Annual Review of Astronomy and Astrophysics*, 51:105–161, jan 2013.

[17] C. M. Casey, S. Berta, M. Béthermin, J. Bock, C. Bridge, D. Burgarella, E. Chapin, S. C. Chapman, D. L. Clements, A. Conley, C. J. Conselice, A. Cooray, D. Farrah, E. Hatziminaoglou, R. J. Ivison, E. Le Floc'h, D. Lutz, G. Magdis, B. Magnelli, S. J. Oliver, M. J. Page, F. Pozzi, D. Rigopoulou, L. Riguccini, I. G. Roseboom, D. B. Sanders, Douglas Scott, N. Seymour, I. Valtchanov, J. D. Vieira, M. Viero, and J. Wardlow. A POPULATION OF z $>$ 2 FAR-INFRARED HERSCHEL -SPIRE-SELECTED STARBURSTS. *The Astrophysical Journal*, 761(2):139, oct 2012.

[18] C. M. Casey, A. Cooray, P. Capak, H. Fu, K. Kovac, S. Lilly, D. B. Sanders, N. Z. Scoville, and E. Treister. A massive, distant proto-cluster at z=2.47 caught in a phase of rapid formation? *The Astrophysical Journal Letters*, 808(2), jun 2015.

[19] Caitlin M. Casey. Far-infrared Spectral Energy Distribution Fitting for Galaxies Near and Far. *Monthly Notices of the Royal Astronomical Society*, 425(4):3094–3103, jun 2012.

[20] Caitlin M. Casey. THE UBIQUITY OF COEVAL STARBURSTS IN MASSIVE GALAXY CLUSTER PROGENITORS. *The Astrophysical Journal*, 824(1):36, mar 2016.

[21] Caitlin M. Casey, Desika Narayanan, and Asantha Cooray. Dusty star-forming galaxies at high redshift. *Physics Reports*, 541(2):45–161, aug 2014.

[22] Caitlin M. Casey, Desika Narayanan, and Asantha Cooray. Dusty star-forming galaxies at high redshift, feb 2014.

[23] Gilles Chabrier. The Galactic Disk Mass Function: Reconciliation of the [ITAL]Hubble Space Telescope[/ITAL] and Nearby Determinations. *The Astrophysical Journal*, 586(2):L133–L136, feb 2003.

[24] S. C. Chapman, A. Blain, R. Ibata, R. J. Ivison, Ian Smail, and G. Morrison. DO SUBMILLIMETER GALAXIES REALLY TRACE THE MOST MASSIVE DARK-MATTER HALOS? DISCOVERY OF A HIGH- z CLUSTER IN A HIGHLY ACTIVE PHASE OF EVOLUTION. *The Astrophysical Journal*, 691(1):560–568, sep 2009.

[25] S. C. Chapman, A. W. Blain, Ian Smail, and R. J. Ivison. A Redshift Survey of the Submillimeter Galaxy Population. *The Astrophysical Journal*, 622(2):772–796, dec 2005.

[26] Yi-Kuan Chiang, Roderik Overzier, and Karl Gebhardt. Ancient Light from Young Cosmic Cities: Physical and Observational Signatures of Galaxy Proto-Clusters. *The Astrophysical Journal*, 779(2), oct 2013.

[27] Shaun Cole, John Helly, Carlos S. Frenk, and Hannah Parkinson. The statistical properties of ?? cold dark matter halo formation. *Monthly Notices of the Royal Astronomical Society*, 383(2):546–556, aug 2008.

[28] Charlie Conroy and James E. Gunn. THE PROPAGATION OF UNCERTAINTIES IN STELLAR POPULATION SYNTHESIS MODELING. III. MODEL CALIBRATION, COMPARISON, AND EVALUATION. *The Astrophysical Journal*, 712(2):833–857, nov 2010.

[29] Elisabete Da Cunha, Stéphane Charlot, and David Elbaz. A simple model to interpret the ultraviolet, optical and infrared emission from galaxies. *Monthly Notices of the Royal Astronomical Society*, 388(4):1595–1617, jun 2008.

[30] Elisabete da Cunha, Fabian Walter, Ian Smail, Mark Swinbank, James Simpson, Roberto Decarli, Jacqueline Hodge, Axel Weiss, Paul van der Werf, Frank Bertoldi, Scott Chapman, Pierre Cox, Alice Danielson, Helmut Dannerbauer, Thomas Greve, Rob Ivison, Alexander Karim, and Alasdair Thomson. An ALMA survey of Sub-millimeter Galaxies in the Extended Chandra Deep Field South: Physical properties derived from ultraviolet-to-radio modelling. *The Astrophysical Journal, article id. 110, 22 pp. (2015).*, 806(1), apr 2015.

[31] E. Daddi, H. Dannerbauer, D. Stern, M. Dickinson, G. Morrison, D. Elbaz, M. Giavalisco, C. Mancini, A. Pope, and H. Spinrad. TWO BRIGHT SUBMILLIMETER GALAXIES IN A z = 4.05 PROTOCLUSTER IN GOODS-NORTH, AND ACCURATE RADIO-INFRARED PHOTOMETRIC REDSHIFTS. *The Astrophysical Journal*, 694(2):1517–1538, oct 2009.

[32] H. Dannerbauer, J. D. Kurk, C. De Breuck, D. Wylezalek, J. S. Santos, Y. Koyama, N. Seymour, M. Tanaka, N. Hatch, B. Altieri, D. Coia, A. Galametz, T. Kodama, G. Miley, H. Röttgering, M. Sanchez-Portal, I. Valtchanov, B. Venemans, and B. Ziegler. An excess of dusty starbursts related to the Spiderweb galaxy. *Astronomy & Astrophysics*, 570, oct 2014.

[33] Ilse De Looze, Maarten Baes, George J. Bendo, Luca Cortese, and Jacopo Fritz. The reliability of [Cii] as an indicator of the star formation rate. *Monthly Notices of the Royal Astronomical Society*, 416(4):2712–2724, oct 2011.

[34] B. T. Draine. Interstellar Dust. *Annual Review of Astronomy &Astrophysics*, 41:241–289, apr 2003.

[35] B.˜T. T. Draine and E.˜E. E. Salpeter. On the physics of dust grains in hot gas. *The Astrophysical Journal*, 231:77, jul 1979.

[36] Eli Dwek. The Evolution of the Elemental Abundances in the Gas and Dust Phases of the Galaxy. *The Astrophysical Journal*, 501(2):643–665, jul 1998.

[37] Duncan Farrah, Vianney Lebouteiller, Henrik Spoon, Jeronimo Bernard-Salas, Chris Pearson, Dimitra Rigopoulou, Howard Smith, Eduardo Gonzalez-Alfonso, David Clements, Andreas Efstathiou, Diane Cormier, Jose Afonso, Sara Petty, Kathryn Harris, Peter Hurley, Colin Borys, Aprajita Verma, Asantha Cooray, and Valentina Salvatelli. Far-infrared Fine-Structure Line Diagnostics of Ultraluminous Infrared Galaxies. *The Astrophysical Journal, Volume 776, Issue 1, article id. 38, 28 pp. (2013).*, 776, 2013.

[38] Robert Feldmann, Eliot Quataert, Philip F. Hopkins, Claude-André Faucher-Giguère, and Dušan Kereš. Colors, Star formation Rates, and Environments of Star forming and Quiescent Galaxies at the Cosmic Noon. *Monthly Notices of the Royal Astronomical Society*, 470(1):1050–1072, oct 2016.

[39] Laura Ferrarese, Richard W. Pogge, Bradley M. Peterson, David Merritt, Amri Wandel, and Charles L. Joseph. Supermassive Black Holes in Active Galactic Nuclei. I. The Consistency of Black Hole Masses in Quiescent and Active Galaxies. *The Astrophysical Journal*, 555(2):L79–L82, jul 2001.

[40] Dan Foreman-Mackey, Jonathan Sick, and Ben Johnson. python-fsps: Python bindings to FSPS (v0.1.1). jan 2014.

[41] J. E. Geach, Y. Matsuda, Ian Smail, S. C. Chapman, T. Yamada, R. J. Ivison, T. Hayashino, K. Ohta, Y. Shioya, and Y. Taniguchi. A submillimetre survey of Lyman ?? haloes in the SA 22 protocluster at z = 3.1. *Monthly Notices of the Royal Astronomical Society*, 363(4):1398–1408, aug 2005.

[42] T. R. Greve, J. D. Vieira, A. Weiß, J. E. Aguirre, K. A. Aird, M. L. N. Ashby, B. A. Benson, L. E. Bleem, C. M. Bradford, M. Brodwin, J. E. Carlstrom, C. L. Chang, S. C. Chapman, T. M. Crawford, C. de Breuck, T. de Haan, M. A. Dobbs, T. Downes, C. D. Fassnacht, G. Fazio, E. M. George, M. Gladders, A. H. Gonzalez, N. W. Halverson, Y. Hezaveh, F. W. High, G. P. Holder, W. L. Holzapfel, S. Hoover, J. D. Hrubes, M. Johnson, R. Keisler, L. Knox, A. T. Lee, E. M. Leitch, M. Lueker, D. Luong-Van, M. Malkan, D. P. Marrone,

V. McIntyre, J. J. McMahon, J. Mehl, K. M. Menten, S. S. Meyer, T. Montroy, E. J. Murphy, T. Natoli, S. Padin, T. Plagge, C. Pryke, C. L. Reichardt, A. Rest, M. Rosenman, J. Ruel, J. E. Ruhl, K. K. Schaffer, K. Sharon, L. Shaw, E. Shirokoff, B. Stalder, S. A. Stanford, Z. Staniszewski, A. A. Stark, K. Story, K. Vanderlinde, W. Walsh, N. Welikala, and R. Williamson. SUBMILLIMETER OBSERVATIONS OF MILLIMETER BRIGHT GALAXIES DISCOVERED BY THE SOUTH POLE TELESCOPE. *The Astrophysical Journal*, 756(1):101, jun 2012.

[43] Tomoki Hayashino, Yuichi Matsuda, Hajime Tamura, Ryosuke Yamauchi, Toru Yamada, Masaru Ajiki, Shinobu S. Fujita, Takashi Murayama, Tohru Nagao, Kouji Ohta, Sadanori Okamura, Masami Ouchi, Kazuhiro Shimasaku, Yasuhiro Shioya, and Yoshiaki Taniguchi. Large-Scale Structure of Emission-Line Galaxies at z = 3.1. *The Astronomical Journal*, 128(5):2073–2079, nov 2004.

[44] C. C. Hayward, P. S. Behroozi, R. S. Somerville, J. R. Primack, J. Moreno, and R. H. Wechsler. Spatially unassociated galaxies contribute significantly to the blended submillimetre galaxy population: predictions for follow-up observations of ALMA sources. *Monthly Notices of the Royal Astronomical Society*, 434(3):2572–2581, jul 2013.

[45] C. C. Hayward, L. Lanz, M. L. N. Ashby, G. Fazio, L. Hernquist, J. R. Martinez-Galarza, K. Noeske, H. A. Smith, S. Wuyts, and A. Zezas. The total infrared luminosity may significantly overestimate the star formation rate of quenching and recently quenched galaxies. *Monthly Notices of the Royal Astronomical Society*, 445(2):1598–1604, oct 2014.

[46] Christopher C. Hayward, Desika Narayanan, Du??an Kere??, Patrik Jonsson, Philip F. Hopkins, T. J. Cox, and Lars Hernquist. Submillimetre galaxies in a hierarchical universe: Number counts, redshift distribution and implications for the IMF. *Monthly Notices of the Royal Astronomical Society*, 428(3):2529–2547, sep 2013.

[47] Wolfgang Hillebrandt and Jens C. Niemeyer. Type Ia Supernova Explosion Models. *Annual Review of Astronomy and Astrophysics*, 38(1):191–230, sep 2000.

[48] B. W. Holwerda. Source Extractor for Dummies v5. *Astronomy and Astrophysics Supplement Series*, 117(2):393–404, jun 2005.

[49] P. F. Hopkins, D. Kere, J. Onorbe, C.-A. Faucher-Giguere, E. Quataert, N. Murray, and J. S. Bullock. Galaxies on FIRE (Feedback In Realistic Environments): stellar feedback explains cosmologically inefficient star formation. *Monthly Notices of the Royal Astronomical Society*, 445(1):581–603, sep 2014.

[50] Philip F. Hopkins. A general class of Lagrangian smoothed particle hydrodynamics methods and implications for fluid mixing problems. *Monthly Notices of the Royal Astronomical Society*, 428(4):2840–2856, jun 2013.

[51] Philip F. Hopkins, Lars Hernquist, Paul Martini, Thomas J. Cox, Brant Robertson, Tiziana Di Matteo, and Volker Springel. A Physical Model for the Origin of Quasar Lifetimes. *The Astrophysical Journal*, 625(2):L71–L74, feb 2005.

[52] Philip F. Hopkins, Eliot Quataert, and Norman Murray. Self-regulated star formation in galaxies via momentum input from massive stars. *Monthly Notices of the Royal Astronomical Society*, 417(2):950–973, jan 2011.

[53] Philip F. Hopkins, Eliot Quataert, and Norman Murray. The structure of the interstellar medium of star-forming galaxies. *Monthly Notices of the Royal Astronomical Society*, 421(4):3488–3521, oct 2012.

[54] Chao-Ling Hung, Caitlin M. Casey, Yi-Kuan Chiang, Peter Capak, Michael J. Cowley, Behnam Darvish, Glenn G. Kacprzak, K. Kovac, Simon J. Lilly, Themiya Nanayakkara, Lee R. Spitler, Kim-Vy H. Tran, and Tiantian Yuan. Large scale structure around a z=2.1 cluster. *The Astrophysical Journal*, 826(2), may 2016.

[55] A. James, L. Dunne, S. Eales, and M. G. Edmunds. SCUBA observations of galaxies with metallicity measurements: A new method for determining the relation between submillimetre luminosity and dust mass. *Monthly Notices of the Royal Astronomical Society*, 335(3):753–761, apr 2002.

[56] Patrik Jonsson, Brent A. Groves, and T. J. Cox. High-resolution panchromatic spectral models of galaxies including photoionization and dust. *Monthly Notices of the Royal Astronomical Society*, 403(1):17–44, mar 2010.

[57] Neal Katz. Dissipational galaxy formation. II - Effects of star formation. *The Astrophysical Journal*, 391:502, jun 1992.

[58] Robert C. Kennicutt. Star Formation in Galaxies Along the Hubble Sequence. *Annual Review of Astronomy and Astrophysics, Volume 36, 1998, pp. 189-232.*, 36:189–232, jul 1998.

[59] Robert C. Kennicutt and Neal J. Evans. Star Formation in the Milky Way and Nearby Galaxies. *Annual Review of Astronomy and Astrophysics*, 50:531–608, apr 2012.

[60] Robert C. Kennicutt, Cai-Na Hao, Daniela Calzetti, John Moustakas, Daniel A. Dale, George Bendo, Charles W. Engelbracht, Benjamin D. Johnson, and Janice C. Lee. DUST-CORRECTED STAR FORMATION RATES OF GALAXIES. I. COMBINATIONS OF Hα AND INFRARED TRACERS. *The Astrophysical Journal*, 703(2):1672–1695, oct 2009.

[61] Robert C. Kennicutt, Jr. The Global Schmidt Law in Starforming Galaxies. *The Astrophysical Journal*, 498(2):541–552, may 1998.

[62] Allison Kirkpatrick, Alexandra Pope, Anna Sajina, Daniel A. Dale, Tanio Diaz-Santos, Christopher C. Hayward, Yong Shi, Rachel B. Somerville, Sabrina Stierwalt, Lee Armus, Jeyhan S. Kartaltepe, Dale D. Kocevski, Daniel H. McIntosh, David B. Sanders, and Lin Yan. A controlled study of cold dust content in galaxies from $z=0-2$. *eprint arXiv:1705.10846*, may 2017.

[63] Pavel Kroupa. The Initial Mass Function of Stars: Evidence for Uniformity in Variable Systems. *Science*, 295(5552):82–91, 2002.

[64] Mark R. Krumholz. The big problems in star formation: The star formation rate, stellar clustering, and the initial mass function, feb 2014.

[65] E. Kuiper, N. A. Hatch, G. K. Miley, N. P.H. Nesvadba, H. J.A. Röttgering, J. D. Kurk, M. D. Lehnert, R. A. Overzier, L. Pentericci, J. Schaye, and B. P. Venemans. A SINFONI view of flies in the Spiderweb: A galaxy cluster in the making. *Monthly Notices of the Royal Astronomical Society*, 415(3):2245–2256, apr 2011.

[66] J. D. Kurk, H. J. A. Röttgering, L. Pentericci, G. K. Miley, W. van Breugel, C. L. Carilli, H. Ford, T. Heckman, P. McCarthy, and A. Moorwood. A Search for clusters at high redshift. I. Candidate Lyalpha emitters near 1138-262 at z=2.2. *Astronomy and Astrophysics*, 358:L1–L4, may 2000.

[67] Claudia del P. Lagos, Tom Theuns, Joop Schaye, Michelle Furlong, Richard G. Bower, Matthieu Schaller, Robert A. Crain, James W. Trayford, and Jorryt Matthee. The Fundamental Plane of star formation in galaxies revealed by the EAGLE hydrodynamical simulations. *Monthly Notices of the Royal Astronomical Society*, 459(3):2632–2650, oct 2016.

[68] R. B. Larson. Turbulence and star formation in molecular clouds. *Monthly Notices of the Royal Astronomical Society*, 194(4):809–826, apr 1981.

[69] Emeric Le Floc'h, Casey J Papovich, Hervé Dole, Eric F Bell, Guilaine Lagache, George H Rieke, Eiichi Egami, Pablo G Pérez-González, Almudena Alonso-Herrero, Marcia J Rieke, Myra Blaylock, Charles W Engelbracht, Karl D Gordon, Dean C Hines, Karl A Misselt, Jane E Morrison, and Jeremy Mould. Infrared Luminosity Functions from the Chandra Deep Field-South: The Spitzer View on the History of Dusty Star Formation at $0 <\tilde{} z <\tilde{} 1$. *The Astrophysical Journal*, 632:169, jun 2005.

[70] A. D. Ludlow, J. F. Navarro, R. E. Angulo, M. Boylan-Kolchin, V. Springel, C. Frenk, and S. D. M. White. The mass-concentration-redshift relation of cold dark matter haloes. *Monthly Notices of the Royal Astronomical Society*, 441(1):378–388, apr 2014.

[71] Piero Madau and Mark Dickinson. Cosmic Star Formation History. *Annual Review of Astronomy and Astrophysics*, 52:415–486, feb 2014.

[72] Crystal L. Martin. Properties of Galactic Outflows: Measurements of the Feedback from Star Formation. *The Astrophysical Journal*, 513(1):156–160, mar 1999.

[73] Tim B. Miller, Christopher C. Hayward, Scott C. Chapman, and Peter S. Behroozi. The bias of the submillimetre galaxy population: SMGs are poor tracers of the most-massive structures in the z 2 Universe. *Monthly Notices of the Royal Astronomical Society*, 452(1):878–883, jul 2015.

[74] Houjun Mo, Frank C. van den Bosch, and Simon White. Galaxy Formation and Evolution. *Galaxy Formation and Evolution, by Houjun Mo , Frank van den Bosch , Simon White, Cambridge, UK: Cambridge University Press, 2010*, 2010.

[75] Benjamin P. Moster, Thorsten Naab, and Simon D. M. White. Galactic star formation and accretion histories from matching galaxies to dark matter haloes. *Monthly Notices of the Royal Astronomical Society*, 428(4):3121–3138, may 2013.

[76] E. J. Murphy, J. J. Condon, E. Schinnerer, R. C. Kennicutt, D. Calzetti, L. Armus, G. Helou, J. L. Turner, G. Aniano, P. Beirão, A. D. Bolatto, B. R. Brandl, K. V. Croxall, D. A. Dale, J. L. Donovan Meyer, B. T. Draine, C. Engelbracht, L. K. Hunt, C.-N. Hao, J. Koda, H. Roussel, R. Skibba, and J.-D. T. Smith. CALIBRATING EXTINCTION-FREE STAR FORMATION RATE DIAGNOSTICS WITH 33 GHz FREE-FREE EMISSION IN NGC 6946. *The Astrophysical Journal*, 737(2):67, may 2011.

[77] Desika Narayanan, Matthew Turk, Robert Feldmann, Thomas Robitaille, Philip Hopkins, Robert Thompson, Christopher Hayward, David Ball, Claude-André Faucher-Giguère, and Dušan Kereš. The formation of submillimetre-bright galaxies from gas infall over a billion years. *Nature*, 525(7570):496–499, sep 2015.

[78] S. Noll, D. Burgarella, E. Giovannoli, V. Buat, D. Marcillac, and J. C. Muñoz-Mateos. Analysis of galaxy spectral energy distributions from far-UV to far-IR with CIGALE: studying a SINGS test sample. *Astronomy and Astrophysics*, 507(3):1793–1813, sep 2009.

[79] Jose Oñorbe, Shea Garrison-Kimmel, Ariyeh H. Maller, James S. Bullock, Miguel Rocha, and Oliver Hahn. How to zoom: Bias, contamination and lagrange volumes in multimass cosmological simulations. *Monthly Notices of the Royal Astronomical Society*, 437(2):1894–1908, may 2013.

[80] Matthew Orr, Chris Hayward, Philip Hopkins, T. K. Chan, Claude-André Faucher-Giguère, Robert Feldmann, Dušan Kereš, Norman Murray, and Eliot Quataert. What FIREs Up Star Formation: the Emergence of the Kennicutt-Schmidt Law from Feedback. *eprint arXiv:1701.01788*, jan 2017.

[81] Roderik A. Overzier. The realm of the galaxy protoclusters: A review, oct 2016.

[82] J. L. Pineda, W. D. Langer, and P. F. Goldsmith. A Herschel [C II] Galactic plane survey. *Astronomy & Astrophysics*, 570:A121, oct 2014.

[83] Francisco Prada, Anatoly A. Klypin, Antonio J. Cuesta, Juan E. Betancort-Rijo, and Joel Primack. Halo concentrations in the standard Λ cold dark matter cosmology. *Monthly Notices of the Royal Astronomical Society*, 423(4):3018–3030, apr 2012.

[84] Dominik A Riechers, C M Bradford, D L Clements, C D Dowell, I Pérez-Fournon, R J Ivison, C Bridge, A Conley, Hai Fu, J D Vieira, J Wardlow, J Calanog, A Cooray, P Hurley, R Neri, J Kamenetzky, J E Aguirre, B Altieri, V Arumugam, D J Benford, M Béthermin, J Bock, D Burgarella, A Cabrera-Lavers, S C Chapman, P Cox, J S Dunlop, L Earle, D Farrah, P Ferrero, A Franceschini, R Gavazzi, J Glenn, E A Gonzalez Solares, M A Gurwell, M Halpern, E Hatziminaoglou, A Hyde, E Ibar, A Kovács, M Krips, R E Lupu, P R Maloney, P Martinez-Navajas, H Matsuhara, E J Murphy, B J Naylor, H T Nguyen, S J Oliver, A Omont, M J Page, G Petitpas, N Rangwala, I G Roseboom, D Scott, A J Smith, J G Staguhn, A Streblyanska, A P Thomson, I Valtchanov, M Viero, L Wang, M Zemcov, and J Zmuidzinas. A dust-obscured massive maximum-starburst galaxy at a redshift of 6.34. *Nature*, 496(7445):329–33, may 2013.

[85] Thomas P. Robitaille. HYPERION: an open-source parallelized three-dimensional dust continuum radiative transfer code. *Astronomy & Astrophysics*, 536:A79, dec 2011.

[86] P. Rosati, P. Tozzi, R. Gobat, J. S. Santos, M. Nonino, R. Demarco, C. Lidman, C. R. Mullis, V. Strazzullo, H. Böhringer, R. Fassbender, K. Dawson, M. Tanaka, J. Jee, H. Ford, G. Lamer, and A. Schwope. Multi-wavelength study of XMMU J2235.3-2557: the most massive galaxy cluster at z > 1. *Astronomy and Astrophysics*, 508(2):583–591, oct 2009.

[87] Mohammadtaher Safarzadeh, Christopher C. Hayward, Henry C. Ferguson, and Rachel S. Somerville. What shapes the far-infrared spectral energy distributions of galaxies? *The Astrophysical Journal, article id. 62, 17 pp. (2016).*, 818(1), aug 2015.

[88] Samir Salim, R. Michael Rich, Stéphane Charlot, Jarle Brinchmann, Benjamin D. Johnson, David Schiminovich, Mark Seibert, Ryan Mallery, Timothy M. Heckman, Karl Forster, Peter G. Friedman, D. Christopher Martin, Patrick Morrissey, Susan G. Neff, Todd Small, Ted K. Wyder, Luciana Bianchi, Jose Donas, YoungWook Lee, Barry F. Madore, Bruno Milliard, Alex S. Szalay, Barry Y. Welsh, and Sukyoung K. Yi. UV Star Formation Rates in the Local Universe. *The Astrophysical Journal Supplement Series*, 173(2):267–292, dec 2007.

[89] Joe Silk and Gary A. Mamon. The Current Status of Galaxy Formation. *Research in Astronomy and Astrophysics*, 12(8):917–946, jul 2012.

[90] James Simpson, Ian Smail, Mark Swinbank, Scott Chapman, James Geach, Rob Ivison, Alasdair Thomson, Itziar Aretxaga, Andrew Blain, Will Cowley, Chian-Chou Chen, Kristen Coppin, Jim Dunlop, Alastair Edge, Duncan Farrah, Edo Ibar, Alex Karim, Kirsten Knudsen, Rowin Meijerink, Michal Michalowski, Douglas Scott, Marco Spanns, and Paul van der Werf. The SCUBA-2 Cosmology Legacy Survey: ALMA resolves the bright-end of the sub-millimeter number counts. *The Astrophysical Journal, Volume 807, Issue 2, article id. 128, 13 pp. (2015).*, 807, may 2015.

[91] Daniel J. B. Smith and Christopher C. Hayward. Deriving star formation histories from photometry using energy balance spectral energy distribution modelling. *Monthly Notices of the Royal Astronomical Society*, 453(2):1597–1607, jul 2015.

[92] Rachel S. Somerville and Romeel Davé. Physical Models of Galaxy Formation in a Cosmological Framework. *Annual Review of Astronomy and Astrophysics*, 53:51–113, dec 2014.

[93] Rachel S. Somerville, Rudy C. Gilmore, Joel R. Primack, and Alberto Domínguez. Galaxy properties from the ultraviolet to the far-infrared: Λ cold dark matter models confront observations. *Monthly Notices of the Royal Astronomical Society*, 423(3):1992–2015, 2012.

[94] Martin Sparre, Christopher C. Hayward, Robert Feldmann, Claude-André Faucher-Giguère, Alexander L. Muratov, Dušan Kereš, and Philip F. Hopkins. (Star)bursts of FIRE: observational signatures of bursty star formation in galaxies. *Monthly Notices of the Royal Astronomical Society*, 466(1):88–104, oct 2017.

[95] Justin Spilker, Daniel Marrone, Manuel Aravena, Matthieu Bethermin, Matt Bothwell, John Carlstrom, Scott Chapman, Tom Crawford, Carlos de Breuck, Chris Fassnacht, Anthony Gonzalez, Thomas Greve, Yashar Hezaveh, Katrina Litke, Jingzhe Ma, Matt Malkan, Kaja Rotermund, Maria Strandet, Joaquin Vieira, Axel Weiss, and Niraj Welikala. ALMA Imaging and Gravitational Lens Models of South Pole Telescope-Selected Dusty, Star-Forming Galaxies at High Redshifts. *The Astrophysical Journal*, 826(2):112, apr 2016.

[96] Volker Springel. Hydrodynamic simulations on a moving Voronoi mesh. *eprint arXiv:1109.2218*, 2011.

[97] Volker Springel. Smoothed Particle Hydrodynamics in Astrophysics. *Annual Review of Astronomy and Astrophysics*, 48:391–430, 2011.

[98] C. Steidel, K. Adelberger, M. Dickinson, M. Giavalisco, M. Pettini, and M. Kellogg. A Large Structure of Galaxies At Redshift z˜3 and its Cosmological Implications. *The Astrophysical Journal*, 492(2):428–438, aug 1997.

[99] Charles C. Steidel, Mauro Giavalisco, Mark Dickinson, and Kurt L. Adelberger. Spectroscopy of Lyman Break Galaxies in the Hubble Deep Field. *Astronomical Journal*, 112:352, apr 1996.

[100] M. L. Strandet, A. Weiß, J. D. Vieira, C. de Breuck, J. E. Aguirre, M. Aravena, M. L. N. Ashby, M. Béthermin, C. M. Bradford, J. E. Carlstrom, S. C. Chapman, T. M. Crawford, W. Everett, C. D. Fassnacht, R. M. Furstenau, A. H. Gonzalez, T. R. Greve, B. Gullberg, Y. Hezaveh, J. R. Kamenetzky, K. Litke, J. Ma, M. Malkan, D. P. Marrone, K. M. Menten, E. J. Murphy, A. Nadolski, K. M. Rotermund, J. S. Spilker, A. A. Stark, and N. Welikala. The redshift distribution of dusty star forming galaxies from the SPT survey. *The Astrophysical Journal Volume 822, Issue 2, article id. 80, 20 pp. (2016).*, 822(2), mar 2016.

[101] L. J. Tacconi, R. Genzel, R. Neri, P. Cox, M. C. Cooper, K. Shapiro, A. Bolatto, N. Bouché, F. Bournaud, A. Burkert, F. Combes, J. Comerford, M. Davis, N. M. Förster Schreiber, S. Garcia-Burillo, J. Gracia-Carpio, D. Lutz, T. Naab, A. Omont, A. Shapley, A. Sternberg, and B. Weiner. High molecular gas fractions in normal massive star-forming galaxies in the young Universe. *Nature*, 463(7282):781–784, 2010.

[102] Yoichi Tamura, Kotaro Kohno, Kouichiro Nakanishi, Bunyo Hatsukade, Daisuke Iono, Grant W. Wilson, Min S. Yun, Tadafumi Takata, Yuichi Matsuda, Tomoka Tosaki, Hajime Ezawa, Thushara A. Perera, Kimberly S. Scott, Jason E. Austermann, David H. Hughes, Itziar Aretxaga, Aeree Chung, Tai Oshima, Nobuyuki Yamaguchi, Kunihiko Tanaka, and Ryohei Kawabe. Spatial correlation between submillimetre and Lyman-α galaxies in the SSA22 protocluster. *Nature*, 459:61, may 2009.

[103] S. Toft, V. Smolčić, B. Magnelli, A. Karim, A. Zirm, M. Michalowski, P. Capak, K. Sheth, K. Schawinski, J.-K. Krogager, S. Wuyts, D. Sanders, A. W. S. Man, D. Lutz, J. Staguhn, S. Berta, H. Mccracken, J. Krpan, and D. Riechers. SUBMILLIMETER GALAXIES AS PROGENITORS OF COMPACT QUIESCENT GALAXIES. *The Astrophysical Journal*, 782(2):68, 2014.

[104] Tomonori Totani, T.T. Takeuchi, Masahiro Nagashima, M.A.R. Kobayashi, and Ryu Makiya. Infrared Spectral Energy Distribution of Galaxies in the AKARI All Sky Survey: Correlations with Galaxy Properties, and Their Physical Origin. *Publications of the Astronomical Society of Japan*, 63:1181–1206, mar 2011.

[105] H. Umehata, Y. Tamura, K. Kohno, R. J. Ivison, D. M. Alexander, J. Geach, B. Hatsukade, D. H. Hughes, S. Ikarashi, Y. Kato, T. Izumi, R. Kawabe, M. Kubo, M. Lee, B. Lehmer, R. Makiya, Y. Matsuda, K. Nakanishi, T. Saito, I. Smail, T. Yamada, Y. Yamaguchi, and M. Yun. ALMA Deep Field in SSA22: A concentration of dusty starbursts in a z=3.09 protocluster core. *The Astrophysical Journal Letters*, 815(1), oct 2015.

[106] Dyas Utomo, Mariska Kriek, Ivo Labbe, Charlie Conroy, and Mattia Fumagalli. Simultaneous Modeling of the Stellar and Dust Emission in Distant Galaxies: Implications for Star Formation Rate Measurements. *The Astrophysical Journal Letters, article id. L30, 6 pp. (2014).*, 783(2), jan 2014.

[107] A. Vale and J. P. Ostriker. Linking halo mass to galaxy luminosity. *Monthly Notices of the Royal Astronomical Society*, 353(1):189–200, feb 2004.

[108] J. D. Vieira, T. M. Crawford, E. R. Switzer, P. A. R. Ade, K. A. Aird, M. L. N. Ashby, B. A. Benson, L. E. Bleem, M. Brodwin, J. E. Carlstrom, C. L. Chang, H.-M. Cho, A. T. Crites, T. de Haan, M. A. Dobbs, W. Everett, E. M. George, M. Gladders, N. R. Hall, N. W. Halverson, F. W. High, G. P. Holder, W. L. Holzapfel, J. D. Hrubes, M. Joy, R. Keisler, L. Knox, A. T. Lee, E. M. Leitch, M. Lueker, D. P. Marrone, V. McIntyre, J. J. McMahon, J. Mehl, S. S. Meyer, J. J. Mohr, T. E. Montroy, S. Padin, T. Plagge, C. Pryke, C. L. Reichardt, J. E. Ruhl, K. K. Schaffer, L. Shaw, E. Shirokoff, H. G. Spieler, B. Stalder, Z. Staniszewski, A. A. Stark, K. Vanderlinde, W. Walsh, R. Williamson, Y. Yang, O. Zahn, and A. Zenteno. EXTRAGALACTIC MILLIMETER-WAVE SOURCES IN SOUTH POLE TELESCOPE SURVEY DATA: SOURCE COUNTS, CATALOG, AND STATISTICS FOR AN 87 SQUARE-DEGREE FIELD. *The Astrophysical Journal*, 719(1):763–783, dec 2010.

[109] J. D. Vieira, D. P. Marrone, S. C. Chapman, C. De Breuck, Y. D. Hezaveh, A. Weiss, J. E. Aguirre, K. A. Aird, M. Aravena, M. L. N. Ashby, M. Bayliss, B. A. Benson, A. D. Biggs, L. E. Bleem, J. J. Bock, M. Bothwell, C. M. Bradford, M. Brodwin, J. E. Carlstrom, C. L. Chang, T. M. Crawford, A. T. Crites, T. de Haan, M. A. Dobbs, E. B. Fomalont, C. D. Fassnacht, E. M. George, M. D. Gladders, A. H. Gonzalez, T. R. Greve, B. Gullberg, N. W. Halverson, F. W. High, G. P. Holder, W. L. Holzapfel, S. Hoover, J. D. Hrubes, T. R. Hunter, R. Keisler, A. T. Lee, E. M. Leitch, M. Lueker, D. Luong-Van, M. Malkan, V. McIntyre, J. J. McMahon, J. Mehl, K. M. Menten, S. S. Meyer, L. M. Mocanu, E. J. Murphy, T. Natoli, S. Padin, T. Plagge, C. L. Reichardt, A. Rest, J. Ruel, J. E. Ruhl, K. Sharon, K. K. Schaffer, L. Shaw, E. Shirokoff, J. S. Spilker, B. Stalder, Z. Staniszewski1, A. A. Stark, K. Story, K. Vanderlinde, N. Welikala, and R. Williamson. Dusty starburst galaxies in the early Universe as revealed by gravitational lensing. *Nature*, 495(7441):344–347, mar 2013.

[110] Mark Vogelsberger, Shy Genel, Volker Springel, Paul Torrey, Debora Sijacki, Dandan Xu, G. Snyder, Simeon Bird, Dylan Nelson, and Lars Hernquist. Properties of galaxies reproduced by a hydrodynamic simulation. *Nature*, 509(7499):177–182, may 2014.

[111] Fabian Walter, Roberto Decarli, Chris Carilli, Frank Bertoldi, Pierre Cox, Elisabete Da Cunha, Emanuele Daddi, Mark Dickinson, Dennis Downes, David Elbaz, Richard Ellis, Jacqueline Hodge, Roberto Neri, Dominik A. Riechers, Axel

Weiss, Eric Bell, Helmut Dannerbauer, Melanie Krips, Mark Krumholz, Lindley Lentati, Roberto Maiolino, Karl Menten, Hans-Walter Rix, Brant Robertson, Hyron Spinrad, Dan P. Stark, and Daniel Stern. The intense starburst HDF 850.1 in a galaxy overdensity at z 5.2 in the Hubble Deep Field. *Nature*, 486(7402):233–236, jun 2012.

[112] Joseph C. Weingartner and B. T. Draine. Dust Grain Size Distributions and Extinction in the Milky Way, LMC, and SMC. *The Astrophysical Journal*, 548(1):296–309, aug 2000.

[113] R. Williamson, B. A. Benson, F. W. High, K. Vanderlinde, P. A. R. Ade, K. A. Aird, K. Andersson, R. Armstrong, M. L. N. Ashby, M. Bautz, G. Bazin, E. Bertin, L. E. Bleem, M. Bonamente, M. Brodwin, J. E. Carlstrom, C. L. Chang, S. C. Chapman, A. Clocchiatti, T. M. Crawford, A. T. Crites, T. de Haan, S. Desai, M. A. Dobbs, J. P. Dudley, G. G. Fazio, R. J. Foley, W. R. Forman, G. Garmire, E. M. George, M. D. Gladders, A. H. Gonzalez, N. W. Halverson, G. P. Holder, W. L. Holzapfel, S. Hoover, J. D. Hrubes, C. Jones, M. Joy, R. Keisler, L. Knox, A. T. Lee, E. M. Leitch, M. Lueker, D. Luong-Van, D. P. Marrone, J. J. McMahon, J. Mehl, S. S. Meyer, J. J. Mohr, T. E. Montroy, S. S. Murray, S. Padin, T. Plagge, C. Pryke, C. L. Reichardt, A. Rest, J. Ruel, J. E. Ruhl, B. R. Saliwanchik, A. Saro, K. K. Schaffer, L. Shaw, E. Shirokoff, J. Song, H. G. Spieler, B. Stalder, S. A. Stanford, Z. Staniszewski, A. A. Stark, K. Story, C. W. Stubbs, J. D. Vieira, A. Vikhlinin, and A. Zenteno. A SUNYAEV-ZEL'DOVICH-SELECTED SAMPLE OF THE MOST MASSIVE GALAXY CLUSTERS IN THE 2500 deg 2 SOUTH POLE TELESCOPE SURVEY. *The Astrophysical Journal*, 738(2):139, jan 2011.

[114] Tiantian Yuan, Themiya Nanayakkara, Glenn G. Kacprzak, Kim-Vy H. Tran, Karl Glazebrook, Lisa J. Kewley, Lee R. Spitler, Gregory B. Poole, Ivo Labbé, Caroline M. S. Straatman, and Adam R. Tomczak. KECK/MOSFIRE SPECTROSCOPIC CONFIRMATION OF A VIRGO-LIKE CLUSTER ANCESTOR AT z = 2.095. *The Astrophysical Journal*, 795(1):L20, oct 2014.